IDAG questions to 4th

Vito Di Benedetto[a], Corrado Gatto[a], Franco Grancagnolo[a],
John Hauptman[b], Anna Mazzacane[a], Giovanni Tassielli[a],
Alexander Mikhailichenko[c], Franco Bedeschi[d]

[a] *INFN and Dipartimento di Fisica, via Lecce-Arnesano, 73100, Lecce, Italy*
[b] *Iowa State University, Ames, IA 50011, USA*
[c] *Cornell University, Laboratory of Nuclear Science, Ithaca, NY, USA*
[d] *INFN and Dipartimento di Fisica, Pisa, Italy*

Guide to these questions and answers

The Contents table will enable you to jump to the question/answer of your choice. To be complete, we have included questions from IDAG before the Tsukuba IDAG meetings in Sec. 1, the questions asked by Paul Grannis and Dan Green in December 2008 in Sec. 2, the Post-Tsukuba questions on 20 April 2009 in Sec. 3 (all concepts) and Sec. 4 (only 4th), and the MDI questions from Nobu Toge on 18 May 2009 in Sec. 5.

Contents

12 June 2009
Version 5.0

1 Pre-LoI Questions (June 22, 2008)

1.1 Sensitivity of different detector components to machine background

1.1.1 Pixel vertex

is strongly dependent on beam debris and designed to reduce occupancy per pixel by a large number of pixels. The inner radius is chosen so that the B=3.5T field suppresses the 2γ background events but, if severe enough, the pixel vertex inner layers will go first. It is unknown (to us) the rate of large radius EM halo debris. However, in all our discussions of vertex chambers over the past four years, no prototype chamber has been beam tested and power-pulsed. It is a common problem.

1.1.2 Cluster-timing tracking chamber

The integration time of the CluCou chamber, corresponding to one BX (350 ns), makes it sensitive to machine backgrounds for only one beam crossing. This is clearly shown in the occupancy plots obtained with the simulated background generated by the Guinea-pig generator.

Moreover, the ultra-low-mass CluCou chamber is particularly immune to IP debris since the cross section for γ-conversion in helium is more than a factor 10^3 smaller than the corresponding one in argon gas mixtures (NIST XCOM, "Photon Cross Sections Database," http://physics.nist.gov/-PhysRefData/Xcom/Test/XCOM.html; "X-Rays Cross Section Compilation," http://cars9.uchicago.-edu/ newville/mcbook/) for γ energies down to 1 keV.

Finally, very low momentum tracks, given the high transverse granularity of the CluCou readout, affect only a limited number of drift cells (tracks with momenta lower than 5 MeV/c have curling trajectories which are fully contained within one single drift cell).

1.1.3 BGO crystal calorimeter

The BGO will absorb predominantly anything electromagnetic (EM). Both the spatial granularity (1×1 cm^2, or 2×2 cm^2) and the GHz-digitization will leave the BGO calorimeter largely unaffected by machine backgrounds. In fact, as noted in the 4th LoI page 37, this detector is designed to be sensitive in ns time slices over its volume to backgrounds of any kind. BGO signals that are out-of-time with respect to the interaction point are clearly flagged. The character of the background (EM or hadronic) can be assessed by the ratio of Čerenkov -to-scintillation light as noted in the LoI Sec. 3.4, pages 54-60.

1.1.4 Fiber calorimeter

The fiber calorimeter is insensitive to backgrounds for the same reasons as the BGO, but more so due to its larger volume and larger radius. In contrast to a multi-mega channel PFA calorimeter, the energy absorbing dual-readout calorimeters *respond directly to energy* and not to individual hits or patterns of hits. This makes 4th more robust against machine backgrounds of any kind.

1.1.5 Muon spectrometer

The muon spectrometer is protected from IP machine background by the deep calorimeters.

The background due to far off-axis machine debris coming down the tunnel, if not properly shielded against, gives either isolated hits in the drift tubes or segments of tracks not pointing to the interaction point. Both of these effects, if synchronous with the BX of interest, can be

easily eliminated off-line. In addition, the $\sigma_t \sim 1$ ns time history of the cluster-timing wires allows rejection of these far-out-of-time tracks.

1.2 Calibration and alignment schemes

For all detectors, there are several stages of alignments: the final geometrical alignments are done with the MONALISA system for which line-of-sight laser beams are required. This system is designed for machine components, but can just as well be used for detector components. The pixel vertex, fiducial locations on the CluCou chamber frame, as well as less critical fiducial marks on the calorimeters can all be aligned with MONALISA.

1.2.1 Pixel vertex

is calibrated by tracks of all kinds, and the calibration ensemble can be filtered down to pure $Z^0 \to \mu^+\mu^-$ for the cleanest possible sample with only prompt tracks.

1.2.2 Cluster-timing tracking chamber: see Sec. 3.2

1.2.3 BGO crystal calorimeter: see Sec. 3.1

1.2.4 Fiber calorimeter: see Sec. 3.1

1.2.5 Muon spectrometer: same as cluster-timing, see Sec. 3.2

1.3 Status of an engineering model

Status of an engineering model describing the support structures and the dead zones in the detector simulation.

We have an engineering model that was presented in Franco Grancagnolo's plenary talk at TILC09 and based within the IDEAS engineering tool that is compatible with the usual array of such tools and developed by A. Miccoli (Engineering Tools CT panel). We comment on each detector in turn:

1.3.1 Pixel vertex

The material supports for the pixel vertex chamber are included in the simulation and amount to 1% X_0. This is twice the amount of material assumed by SiD and ILD, each with 0.5% X_0.

1.3.2 Cluster-timing tracking chamber

The engineering model for the CluCou chamber is fully described in a mechanical engineering thesis (A. Santaloia, Problemi strutturali di un rivelatore di particelle, Universit del Salento, Facolt di Ingegneria, Laurea in Ingegneria Meccanica, Lecce, 2008). All details of the chamber structure have been studied and a finite element analysis of the model has been performed to calculate the maximum deformations of the structure under the stress of the field wires. Consequently, a wiring strategy has been devised which takes into account, and corrects for, the plate deformations occurring during the wiring procedures.

The total weight of the CluCou chamber, including front-end electronics cards, HV and signal cables, amounts only to hundreds of kg.

Conceptually, the chamber is suspended through three longitudinal C-fiber rails placed azimuthally at 120 degs. from each other and grown out of the outer surface of the gas containing outer panels (12 of them) of CluCou. The chamber slides inside corresponding tracks supported by the C-fiber structure holding the inner side of the BGO crystal calorimeter. The material of the rails and of the tracks is not simulated in our montecarlo as lumped material, but it is taken into account by considering it as uniformly spread out on the outer CluCou panels (5 mm C-fiber total) and on the inner structure of the BGO crystal calorimeter (1 cm C-fiber total).

1.3.3 BGO crystal calorimeter

The BGO has been studied by Alessandro Miccoli and consequently 1 cm of carbon fiber has been included to simulate the crystal supports, and 0.5 cm of silicon to simulate the electronics. These are uniform amounts of material, not lumped. Please see Sec. 4.1 for figures.

1.3.4 Fiber calorimeter

The edges of the fiber modules are very realistic, and in fact every fiber is individually included in the GEANT4 geometry inside ILCroot. The support brackets at the back of the truncated pyramid modules are not included, but at the end of 9-10 $\lambda_{\rm int}$ this is negligible and not critical to physics. The design of the truncated pyramid modules is fully hermetic with modules supported from the rear.

1.3.5 Muon spectrometer

Detailed design drawings were shown in F. Grancagnolo's TILC09 talk, and also in the DOD (March 2007). All supports, made of Al, have been properly dimensioned although they have not been simulated in our montecarlo, since these materials are much less critical behind the calorimeter.

1.4 Plans for getting the necessary R&D results

Plans for the necessary R&D to transform the design concept into a well-defined detector proposal are listed in the LCRD proposal to DoE/NSF in February 2009. The LCRD funds from DoE-NSF are intended to support university groups in detector development in collaboration with Fermilab. These funds are the only mechanism for funding 4th work. If 4th is not funded even at a minimal level, then you will not see the "necessary R&D results" from 4th.

1.5 Push-pull ability with respect to technical aspects

"The push-pull ability with respect to technical aspects (assembly areas needed, detector transport and connections) and maintaining the detector performance for a stable and time-efficient operation" has been addressed in the Note "4th Concept statement on the proposed push-pull detector configuration at the ILC" which we reproduce here. In the next section, we address all items in the MDI document "Functional Requirements on the Design of the Detectors and the Interaction Region of an e^+e^- Linear Collider with a Push-Pull Arrangement of Detectors," B.Parker, *et al.*.

1.5.1 4th Statement on Push-Pull: 13 Dec 2006

4th Concept statement on the proposed

push-pull detector configuration at the ILC

A. Mikhailichenko and J. Hauptman

December 13, 2006

Abstract

The 4th Concept detector is modular and light-weight by virtue of the dual solenoid flux return that allows for an iron-free detector. The only mass of any importance in the detector is the calorimeter mass, about 10 interaction lengths equivalent of brass over 4π starting at a radius of $r \approx 1.5$ meters. We do not see any show-stoppers in a properly engineered realization of push-pull for the 4th concept. The level of confidence can be high with engineering foresight. The final quadrupoles will be supported by the detector itself to greatly decrease the incoherent beam motion due to ground motion and vibration, and for near-IP control of the final beam aim and focus. Active tuning, mechanical and electromagnetic correction coils, would allow for a quick restoration of luminosity. The detector itself will have a modest number of channels in the triple-readout calorimeter, about 20K, and we anticipate on-detector electronics to compress the final cable count of the pixel vertex and TPC detectors. We do not believe that this will be easy, and the caution expressed by the GLD and LDC groups is warranted in the absence demonstrated feasibility with sufficient confidence. In addition to the move time, the Z^0-calibration running time after each move is essentially a luminosity loss.

Specific considerations

We list here several specific considerations for the 4th concept detector and some more general assumptions and suggestions for all concept detectors.

1. The 4th concept mass is about 900t, less than an iron-based large detector at about 13,000t. Therefore, initial considerations for rapid detector movements at an interaction point, such as floor deformations, are minimal and many other issues of strengths and supports during motion are alleviated;

2. The FF lenses delivering low-β at the IP are carried by the detector, and therefore the compensation of the movement of the beam-delivery system elements are not a large problem for the 4th concept;

3. Beam-based alignment includes electrical and mechanical adjustment of FF optics attached to detector and this procedure is an intrinsic element of functioning of 4th;

4. the 4th detector does not provide the necessary radiation shielding of personnel, however the $10\lambda_{\rm int}$ calorimeter in combination with movable concrete walls, as has been suggested by the push-pull study group, may be sufficient;

5. All power, water, cryogenics, and data cables are attached to the detector so that easy motion is possible without reconnection;

6. Vibration isolation and protection are arranged by attaching the final beam telescope to the detector, so a push-pull scenario does not affect it at all;

7. It is assumed that each detector has its own set of final focus elements, and that a common point can be found to break the beam lines.

8. It is assumed that the beam line is broken at common points for the detectors by valve pairs and pump outs. The design of the beam delivery optics will allow one to break the beam

delivery channel practically at any point and the design of a low loss connection is not a problem;

9. We anticipate that dump resistors and other apparatus associated with the superconducting magnets are carried by the detectors;

10. We suggest that, to keep open the possibility for operation of two detectors simultaneously at some time in the future, the service tunnel must be located far enough from the main beam tunnel, so that if a decision for simultaneous operation is made, the service tunnel could be filled with focusing elements for the second beam delivery line with minimal cost.

General comments

The large iron-blanketed detectors GLD, LDS, SiD were designed, as was 4th, without consideration of frequent detector movement, and therefore new and unfamiliar ideas might be required for a comfortable solution to push-pull such as already outlined in the note "The Meaning of Push-Pull". In addition, the newest ideas about design of the FF beam delivery lines may bring the length and cost of the lines down to an acceptable level compared with the expenses associated with frequent motion of heavy (∼13000t) but delicate equipment, especially since the costly FF lenses belong to the detector.

Summary

We will continue to study this question, and rethink the construction and maintenance of each detector subsystem, but at the present time we are comfortable with the proposed push-pull scheme.

1.5.2 "Functional Requirements ... ", ILC-Note-2009-050, 30 April 2009

Note that we are signatories on this Functional Requirements document; there is no conflict or incompatibility between 4th and the IR/push-pull schemes. These questions somewhat overlap the later questions in Sec. 5.

We respond to each item addressed in the note "Functional Requirements on the Design of the Detectors and the Interaction Region of an e^+e^- Linear Collider with a Push-Pull Arrangement of Detectors," B.Parker (BNL), A.Mikhailichenko (Cornell Univ.), K.Buesser (DESY), J.Hauptman (Iowa State Univ.), T.Tauchi (KEK), P.Burrows (Oxford), T.Markiewicz, M.Oriunno, A.Seryi (SLAC), ILC-Note-2009-050 (30 April 2009).

Final Doublet QD0 moves with detector, and this is no problem for 4th. In addition (see footnote 1 of this report), we want to also carry QF1 on the detector to greatly reduce the beam-to-beam spatial variations. This is like putting all optical elements on the same optical bench, rather than having them on different benches. MDI people agree the 4th design is better, and we know it is better. Mikhailichenko has done a calculation (see 4th LoI Appendix A, "A.MDI-Mikhailichenko-stability-final-doublet-lenses.doc") in which it is clear that this is necessary. Hence, all final focus elements and the detector are "one piece" in the 4th design.

Elapsed time for an exchange of detectors has not been estimated by us (yet). We believe it must be comparable or less than ILD or SiD, since 4th is a simpler detector, smaller in transverse dimension, and lighter by 10 kt.

Vacuum ports: no problem.

Beam Feedback System presents no problem to 4th since our forward region is un-encumbered by iron mass. We can operate at all reasonable L^*, and QD0 and QF1 are mounted inside the central support pipe with is part of the detector itself. The BPM are also mounted here.

Beam-beam parameter space has not been studied by us. This mostly affects the pixel vertex chamber, and no concept has yet tested such a chamber. We are thinking of ways to solve this problem by designing a new, smaller vertex chamber that is much less sensitive to the specific beam conditions.

QD0 support and alignment is easy in 4th, again, because we have a single support structure for all final focus elements and an open geometry in which sophisticated alignment systems such as MONALISA can be easily incorporated.

The return of the detector after a push-pull to mm spatial accuracy and 100 μrad angular accuracy is not a problem. Subsequent alignments are by active and passive movers as stated in the 4th LoI and as tested by Mikhailichenko, *et al.*, in the FFTB (Final Focus Test Beam, *Phys. Rev. Lett.* **74**:2479-2482,1995).

Length of IR perpendicular to beam is not a problem. 4th is comparable to or smaller than ILD and SiD.

Beam height 9.5 m above cave floor (Fig. 38).

Radiation environment has been calculated by T. Sanami and reported in the LoI. We can easily shield the off-beam detector and its personnel. We will make this shielding useful as an additional detector for the 4th facility. It should be noted at this point that only 4th leaves a low neutron dose in the IR, because we absorb the neutrons by $np \rightarrow np$ scattering as part of our calorimeter signal. Both ILD and SiD (consisting of high Z, A materials) have no neutron moderation.

Magnetic environment in 4th is completely controllable and, for example, the fringe field of 4th is zero outside the detector. We are far below even the lowest allowed field in the IR. This is fundamentally the result of having an iron-free detector.

1.5.3 Quenches of the dual solenoids

The question was raised at the TILC09 MDI session about what happens when one solenoid quenches and the other does not. This is not a problem since we will turn off the un-quenched solenoid and inductively control the rate of decrease of current so that the zero-fringe-field condition remains at all times. There are actually many solutions to this problem, but we know that we can keep the field in the IR outside the detector below the limits throughout a quench.

1.6 A short statement about the energy coverage

The energy "coverage" of 4th is excellent and already capable of doing physics at CLIC, primarily because the calorimetry is demonstrated to be linear (Fig. 1) and the muon spectrometer resolution is excellent. The deterioration of the performance at energies higher than 500 GeV mainly affects tracking. We list potential upgrades for each system.

1.6.1 Pixel vertex

No change; but attention must be paid to higher backgrounds and higher background rates. We can lean on Moore's Law and glibly claim that silicon monolithic pixel vertex chambers will improve. An obvious upgrade is readout within one beam crossing to reduce all backgrounds.

1.6.2 Cluster-timing tracking chamber

Serious considerations about the operability of a tracking detector based on cluster counting/timing at higher center-of-mass energies can only be made after detailed knowledge of the beam time structure and of the nature and amount of machine backgrounds.

Issues concerning cell occupancy and track separation are of utmost importance here. We show in Sec. 4.2, however, that at 500 GeV center-of-mass energy and in the case of the largest multiplicity events, like $t\bar{t}$ production, neither efficiency, nor resolutions are affected when the hits belonging to the second track in a cell are switched off. Not even when the space point resolution is doubled from 50 μm to 100 μm. This is a good indication of the robustness of the CluCou tracking solution at ILC energies.

An extrapolation of the tracking performance to CLIC energies necessarily requires detailed simulation studies and chamber parameters optimization, which we intend to undertake as soon as possible.

1.6.3 BGO crystal calorimeter

No problem; except, we would need to extend the dynamic range of the photo-converter/digitizer combination.

1.6.4 Fiber calorimeter

No problem, see linearity plot in LoI, Fig. 17, p. 30, included here as Fig. 1. However, we will need to augment the dynamic ranges of the photo-converter and the digitizer. This is not a difficult problem.

1.6.5 Muon spectrometer

We would be more careful with alignment and spatial resolutions of the cluster-timing chambers. This muon spectrometer already has excellent resolution for all tracks exiting the calorimeter and solenoid, at least a factor of 10 better precision than for an iron-based system, but if we wanted to extend its momentum reach by a factor of two, we would need a factor of four in spatial/alignment precisions. This would be difficult, but there are several possible solutions.

1.7 How was the detector optimized:

How was the 4th detector optimized, for example the identification of the major parameters which drive the total detector cost and its sensitivity to variations of these parameters.

The first fundamental optimization of 4th was the design and successful beam tests of its two essential systems: calorimetry and tracking. These published and understood results (DREAM calorimeters, and KLOE tracker plus cluster timing) are existence proofs that, effectively, remove from the table unworkable and inferior options. It is relatively easy to move from a working instrument, whose strengths and limitations are understood, to an optimum instrument. There are many

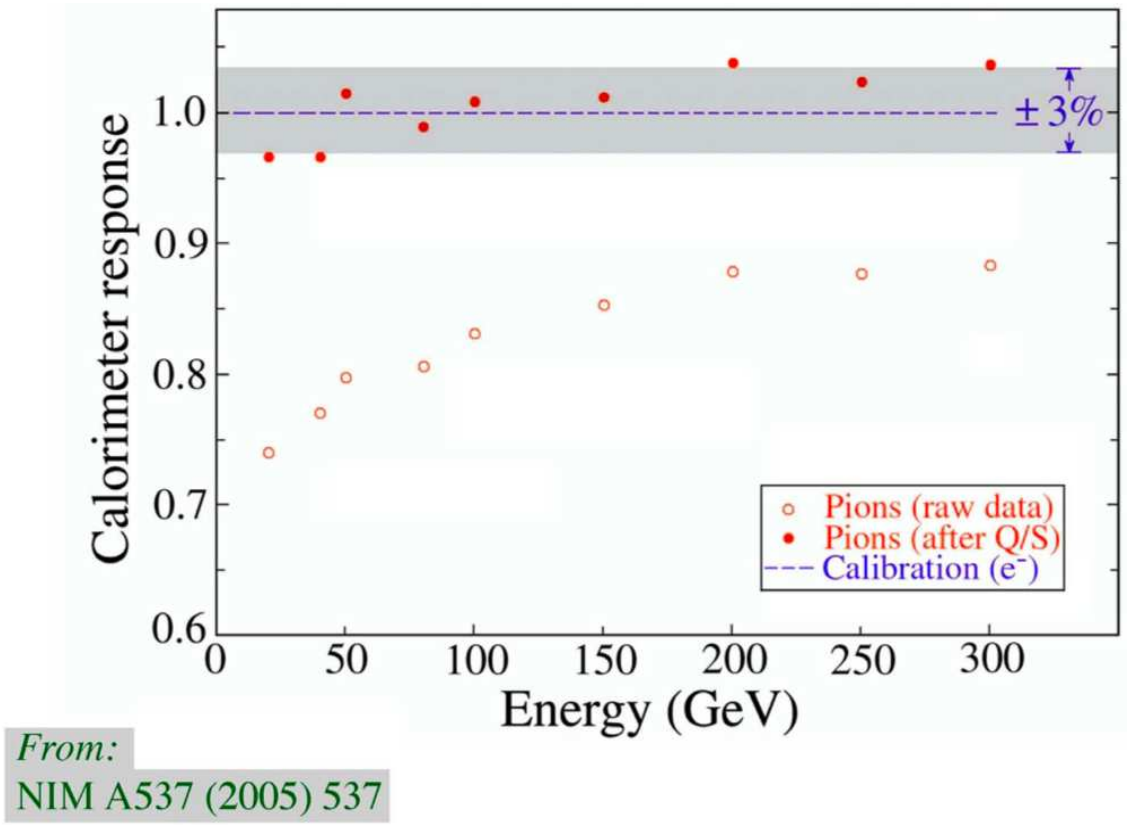

Figure 1: Hadronic calorimeter linearity, measured in CERN beam tests, from 20 to 300 GeV.

illustrations noted in our numerous publications and talks at ILC meetings on the optimization of both cluster-timing tracking and dual-readout calorimetry.

The second fundamental consideration in the design of a big detector (in our view) is that *each detector component must be independent of other detector components and independently optimized itself.* Specifically, this means that

1. the calorimeter basic measurements of energy must not depend on the tracking system.
2. the tracking detector must not rely on the calorimeter, or even the vertex chamber, for finding tracks. The tracker must have high efficiency and high precision in finding tracks throughout its volume without assistance.
3. muon measurement and identification necessarily depends on both tracking and non-absorption. In 4th, we have gone one step further than any other detector: the dual-readout fiber calorimeter provides an *independent* muon identification without reference to tracking or energy measurement.

The combination of detector components in the measurements of partons (jets, e, μ, π) then results in a greatly superior overall detector in which these separate individually capable components reinforce each other. Therefore, the major parameters were optimized as follows:

- **tracking:** the existing KLOE chamber has operated for 10 trouble-free years, and we base the geometry of CluCou on this design, with our well-tested cluster-timing electronics as an

augmentation to its physics performance. From KLOE and our tests, we know that a track length of 1.3 meters gives us the resolution we require, along with dE/dx measurement and calibration robustness, and we take the tracking chamber from 0.2 meters to 1.5 meters. The length of CluCou is not yet fixed, although we did fix it for the benchmark event simulations. The cost is given in the 4th LoI (page 105, Fig. 119) and for a fixed cell size, the cost goes like

$$\text{tracking cost} = \$12M + \$12M \times (R_{\text{trk}}/1.5m)^2$$

since half the \$24M cost of CluCou is the timing and digitizing electronics.

- **calorimeter depth:** the DREAM module is 10 λ_{int} deep over 2 meters. With some consolidation of volume, we can achieve 9 λ_{int} in 1.5 meters, and we are fully confident of its physics performance, that is, we know the relationships between fiber volumes, photo-electron yields, numerical apertures, attenuations, *etc.*, on the calorimeter performance. For fixed angular granularity, the number of channels is fixed and the cost depends on the volume of brass and the length of fiber, since there is one depth section with outer radius R_{calor},

$$\text{calorimeter cost} = \$99M + \alpha(R_{\text{calor}}/3.0)^2 + \beta(R_{\text{calor}}/3.0),$$

  where α is for brass and β is for fibers.

- **dual-solenoids:** Sec. 1.9 contains a comparison of the costs of a second solenoid to the iron return yoke. We could use the PDG formula for the cost of a superconducting solenoid as a function of stored energy as

$$\text{dual} - \text{solenoid cost}(\$) = 0.532 \cdot [W(MJ)]^{0.662},$$

  and where the stored energy goes like $W \approx B^2R^2L$. For 4th's dual solenoids, there are two of each, but the right way to think is that the inner solenoid is hard (precision, pushing current density limits), but the outer solenoid is easier (no real precision required, much lower current densities, and lower forces).

The crystal BGO calorimeter is not optimized. We have put $1\times1\text{cm}^2$ crystals into the simulation so that we can study lateral segmentations of $1\times1\text{cm}^2$, $2\times2\text{cm}^2$, and $3\times3\text{cm}^2$. Presently, the cost is large (\$99M), but we intend to substitute BSO (Bismuth Silicate) or BBO (Bismuth Borate) for the very expensive BGO with small loss to the dual-readout capabilities.

These are the reasons why 4th was so easy to design, and why the physics results are so good. We are not required to design a tracking system around a PFA calorimeter, or to use a 'stub' in a PFA calorimeter to find Λ, K^0 in a tracking system.

The optimization of 4th was discussed in Sec. 2.2 of the LoI in general terms. Detailed optimization awaits more time and resources (requested in LCRD DoE/NSF proposal). The procedure we can follow to optimize the detector is summarized here in simple terms:

a. choose a physics process specifically dependent on one detector (*e.g.* tracking, calorimetry, muon, or vertex);

b. define a "physics quality" measure for this process (*e.g.* σ, BR, mass);

c. vary gross physical dimensions by 20% (inner and outer radii $R_{\text{tracker}}, R_{\text{calorimeter}}, R_{\text{solenoid}}$);

d. keep constant the *known and measured* performances of cluster-timing and dual-readout;

It is then an easy task to plot "physics quality" *vs.* gross parameter and pick an optimum; it is an exceedingly difficult task to decide on an optimum when physics processes conflict, as they must for tracking *vs.* calorimeter performance. In the end, it will be a judgment. There is a very different approach to optimization: after the single-detector optimizations are complete, ask what physics is weakened or compromised by a design change. Again, one is left with a judgment call. This procedure is very highly compute intensive, but ILCroot is designed with this problem in mind, and we have requested LCRD DoE/NSF funds through TTU for its completion.

1.8 Plan to develop the forward tracking design?

What is your plan to develop the forward tracking design? What are the impacts of added silicon disks either within or outside the tracking chamber enclosure? How would forward toroidal magnets improve forward momentum resolution, and how would they be integrated?

We intend to study exactly this: the impact of silicon on tracking overall in 4th. There are many challenges ahead for silicon systems, and several very capable groups are solving these problems, *e.g.*, the SiLC collaboration that works with the 4th group. These challenges are

- power cycling is required to forestall liquid cooling, in turn to keep the mass low;
- silicon has mass and a radiation length budget. The silicon systems of both ATLAS and CMS are far beyond any intended goal for limitation of the radiation length budgets, and reach 1.4 X_0 and 6.0 X_0 for CMS and ATLAS, respectively, as seen in Fig. 2. This presents a challenge that cuts across several often weakly connected disciplines: mechanical support engineering, physics needs, connectors, power delivery, cabling, overall assembly. These tasks may be done by different people, not realizing fully the needs of others;
- silicon systems have a large number of channels, requiring on-board electronics to filter and zero suppress; and,
- the precision (typically 5μm) alignments required are to be tested, and these tests will address the slow mis-alignments induced in push-pull situations.

These issues are not simple, and much R&D is required. We support this R&D, in particular the work that has been recently framed by Ron Lipton in the Detector R&D Common Task Panel. This outcome of too much material may be pre-ordained by the nature of the building of a large detector. We need to understand this before embarking on a silicon system, even if only in the forward region; and, finally, even for a high spatial precision silicon system in the forward region, the momentum resolution is degraded completely as the tracks become parallel to B, and scales as $\sigma_p/p^2 \propto 1/\sin^{5/2}\theta$. (One power for $v \times B$, one power for track length, and the square-root for the number of measurements.)

The last point begs for a new solution to the whole forward region (we are indebted to Chris Damerell who made this clear at the Beijing Tracking Review). A toroid with an azimuthal field that goes like $B_\phi \sim 1/r$ will give a radial kick ($F_r \propto v_z \times B_\phi$) to charged particles, and can solve this problem providing:

1. the cryostat is thin (it has to be superconducting, BINP has built such thin solenoids);
2. the calorimeter is not compromised too much relative to the tracking gain (this is a hard problem);

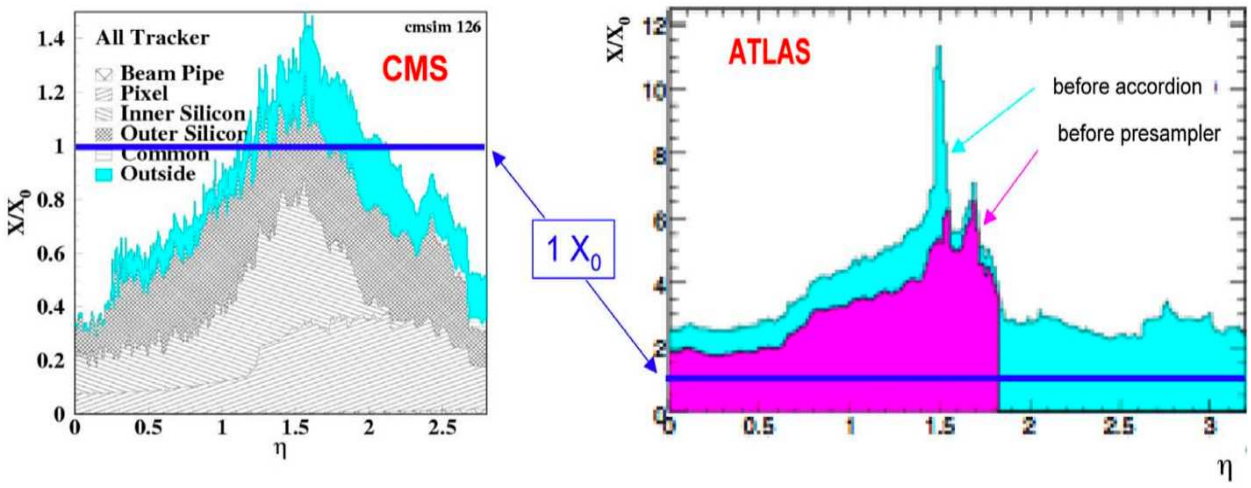

Figure 2: Tracking system silicon material budgets for CMS and ATLAS. A direct comparison with ILC concept detector is not a fair or useful comparison, although the tendency of low-mass systems to creep up to high masses is a problem to be watched.

3. there is space between CluCou and the calorimeter; and,

4. the necessary spatial resolutions can be achieved for measuring the radial bend angle in the toroidal field.

Clearly, this whole problem requires some time and thinking, and with ILCroot we have the tools to make this study. We are not ready to specify a design, and for this reason we have left the forward region inside 8-degree out of the LoI design and the benchmark processes. We will do *even better* when we fill this region with an intelligent detector.

1.9 Compare dual solenoids with iron yoke

Can you compare the benefit to physics, cost, and MDI complexity for a dual solenoid approach compared with one with iron return yokes. Is the dual solenoid an optimized choice? Is there demonstrable physics benefit from a second muon momentum measurement over outer muon identification with its momentum taken from the inner tracker?

First, there are several questions of different kinds (MDI, fringe fields, final focus (FF), push-pull weight, $\gamma\gamma$ collisions) linked together in this one envelope. Of course, exactly the same questions could be addressed to the traditional detector approach (with iron yoke). The first question is essentially to compare the same 4th detector, but with iron yoke instead of the second solenoid. The question can also mean a comparison of 4th with the other two LoI detectors, a question which is addressed in the 4th LoI (although we purposefully did not directly compare to other detectors since that is not our place).

First, comparison of cost: Cost of steel[1] is about \$900/t so 15kt will cost \$13.50M. The tooling, handling must be added to this amount which doubles the price, so \$26M is the total cost of the

[1]See, for example, http://www.steelbb.com/steelprices.

yoke. Add here installation, and total cost easily comes to $30-40M. The cost of a second solenoid could be expected at about $20M as it is simpler than the central one; the field generated by this solenoid is about 1.5T, so the problems associated with strength are less severe for this solenoid as the pressure drops quadratically with magnetic field reduction (1T is 4atm). This solenoid will be sectioned and assembled on-site at ground level above detector cave. So the total savings comes to $10M to use a solenoid instead of iron yoke. The absence of iron makes installation of forward tracking arranged with toroidal magnet easier. We are considering this magnet made with SC cable.

Second, MDI complexity: At first sight there is no difference in cost, but iron-free approach makes visible all elements of detector from one point. From the point of alignment after energizing the solenoid, when ponderomotive forces bend elements of detector magnet (with or without iron), this benefit of no-iron becomes vital. Specifically, the MONALISA alignment scheme requires line-of-sight holes through the detector, which is not easy with a 10-ft thick iron yoke. These forces move parts of the CMS detector (e.g, HF) by 19 mm at a distance of 11 meters from the IR. Such displacements of parts of a detector are not acceptable for a precision detector at a linear collider.

More importantly, the absence of iron makes the interaction of the field generated by the FF lenses with it surroundings less intensive, and tuning these FF elements by changing their currents in coils does not deflect their positions or put any forces on them in an iron-free detector. These FF elements, QF1 and QD0, should not find themselves in an un-tunable magnetic environment defined by iron. In the case of iron, some lenses are in the vicinity of iron and might be affected by ponderomotive attraction. So strictly speaking, the absence of iron makes MDI problems easier in all instances covered by the MDI document.[2]

As far as precision measurement of muon momenta after the calorimeter, this allows an energy balance between tracker-calorimeters-muon spectrometer that rejects by a factor of 30-50 the pion background relative to muon signal. Resolution is always worth having.

Dual solenoids are an optimal choice not only for ILC, but for any future detector with a high (4-5T) solenoidal field. The detailed structure of coils is under development as we lower the peak field at the conductors, and also the stored energy, but the general concept, we believe, is optimal. So, yes, the 4th benefits from a dual solenoid. Although 4th could be realized with an iron yoke, the second solenoid makes for a more elegant experimental solution; this elegance is expressed in cost savings, better physics, less risk to FF optics, and easier operational functionality associated with the absence of a heavy iron yoke.

[2]B.Parker, *et al.*, Functional Requirements on the Design of the Detectors and the Interaction Region of an e^+e^- Linear Collider with a Push-Pull Arrangement of Detectors, ILC Note-2009-050.

2 Question on dual-readout calorimetry: Paul Grannis, Dan Green (10 Dec 2008)

Q1. *Does the dual readout calorimetry require an energy dependent calibration for the low momentum range of particles?*

Another issue is particle species dependence of the response. Data is available from the CMS test beam work done in the CERN H2 beam line. The response as a function of beam momentum for a combined ECAL + HCAL calibrated on electrons is shown below. There is a substantial dependence for different species. Presumably, the difference of pions to protons has to do with the leading particle effect for pions a neutral pion contributing to f_0 while for protons a leading neutron which does not yield electromagnetic energy. This behavior may mean that the f_0 which is found event by event has a different magnitude and energy dependence for different particle species.

Mean response in energy to the CMS ECAL+HCAL, calibrated on electrons, for different particle species as a function of beam momentum.

The Kaon and proton response is rather different from the pion response. Note that this is true at the highest available energy - 350 GeV for protons. Therefore, treating the calorimetry with a single e/h ratio might introduce mis-measures in the energy without ancillary particle id information being used.

Q2. *The question for the experimenters is: Does the experiment consider species dependent response of the dual readout calorimeter?*

2.1 Species dependence of dual-readout calorimeter response (Q2)

The response of the CMS calorimeters (ECAL+HCAL+OH?) is shown *vs.* beam momentum in the left frame of Fig. 3. Momentum is the wrong variable. It is clear and obvious that a proton with kinetic energy $KE = 2$ GeV can deposit *at most* 2 GeV in the calorimeter medium by dE/dx. In contrast, an anti-proton with $KE = 2$ GeV can deposit its kinetic energy *plus* $2M_pc^2$ of annihilation products. The physically correct variable is *available energy*, that is, the energy that can appear as a calorimeter signal. The identically same data plotted *versus* available energy is shown in the right frame of Fig. 3.

> There is no appreciable species dependence to the signals measured in the calorimeter, when proper accounting of available energy is made.

If one is concerned about the various species of particles appearing in QCD jets, a simple argument from energy conservation shows that, for example, the production of a proton-antiproton pair during the fragmentation process inside the jet will subtract $2M_pc^2$ in energy from the jet, and this same $2M_pc^2$ will be given back as calorimeter energy when the anti-proton annihilates in the calorimeter. Energy is conserved from the quark/gluon to the calorimeter signal.

There remains in Fig. 3 an energy-dependence to the calorimeter response that is addressed in the next section.

2.2 Momentum dependence of dual-readout calorimeter response (Q1)

The average π^- response in Fig. 3 has unsurprising similarities to the non-dual-readout response of the DREAM module, that is, just the scintillation (S) signal, shown in Fig. 17 of the LoI (page 30) included here as Fig. 1. In the single-readout scintillation π^- response in DREAM , the S signal falls from 90% down to 70% going from high energies (300 GeV) to 20 GeV. The details of the

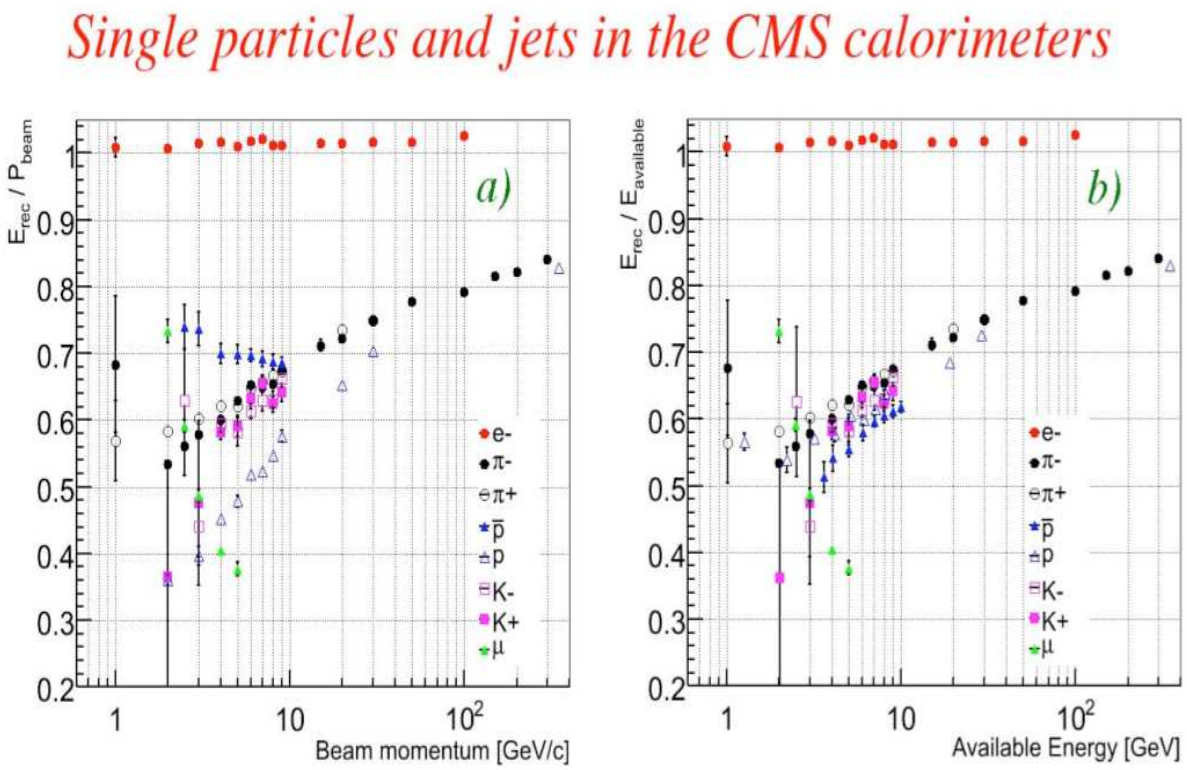

Figure 3: Response of the CMS calorimeters (ECAL+HCAL+OH) to $e^-, \pi^\pm, p, \bar{p}, K^\pm$, and $\mu^\pm$ from 2 GeV/c to 300 GeV/c beam momentum (left frame), and the same data plotted *versus* available energy in GeV (right frame).

magnitude and energy dependence are different because these are two very different calorimeters with different sampling fractions, *etc.*, but the main physical dependence is the same (as it should be). The CMS data for the pion response with energy, with the jet response added, is shown in Fig. 4.

There are three *fundamental* facts to understand here:

- the relative EM to "hadronic" response, called "(e/h)", is greater than one, $(e/h) > 1$, in this CMS calorimeter and, therefore, neither of these curves for π^- or jet (Fig. 4) will reach a response of 1.0;
- the average EM fraction is an increasing function of hadron energy since the production of π^0 in successive generations of hadronic interactions results only in EM calorimeter signals and, therefore, the average hadronic response will increase with energy simply because the EM fraction is increasing and $(e/h) > 1$; and,
- the value of (e/h) for a calorimeter is the averaged relative response over *the entire hadronic shower*, from the initial particle to the final low-energy remnants of the shower. It cannot be applied just to the low-energy remnants without producing nonsense results.

The meaning of *an entire hadronic shower* is that particles are being produced in the showering processes, such as $\pi^\pm$, spallation protons, MeV neutrons, energetic neutrons and protons, K's, etc.

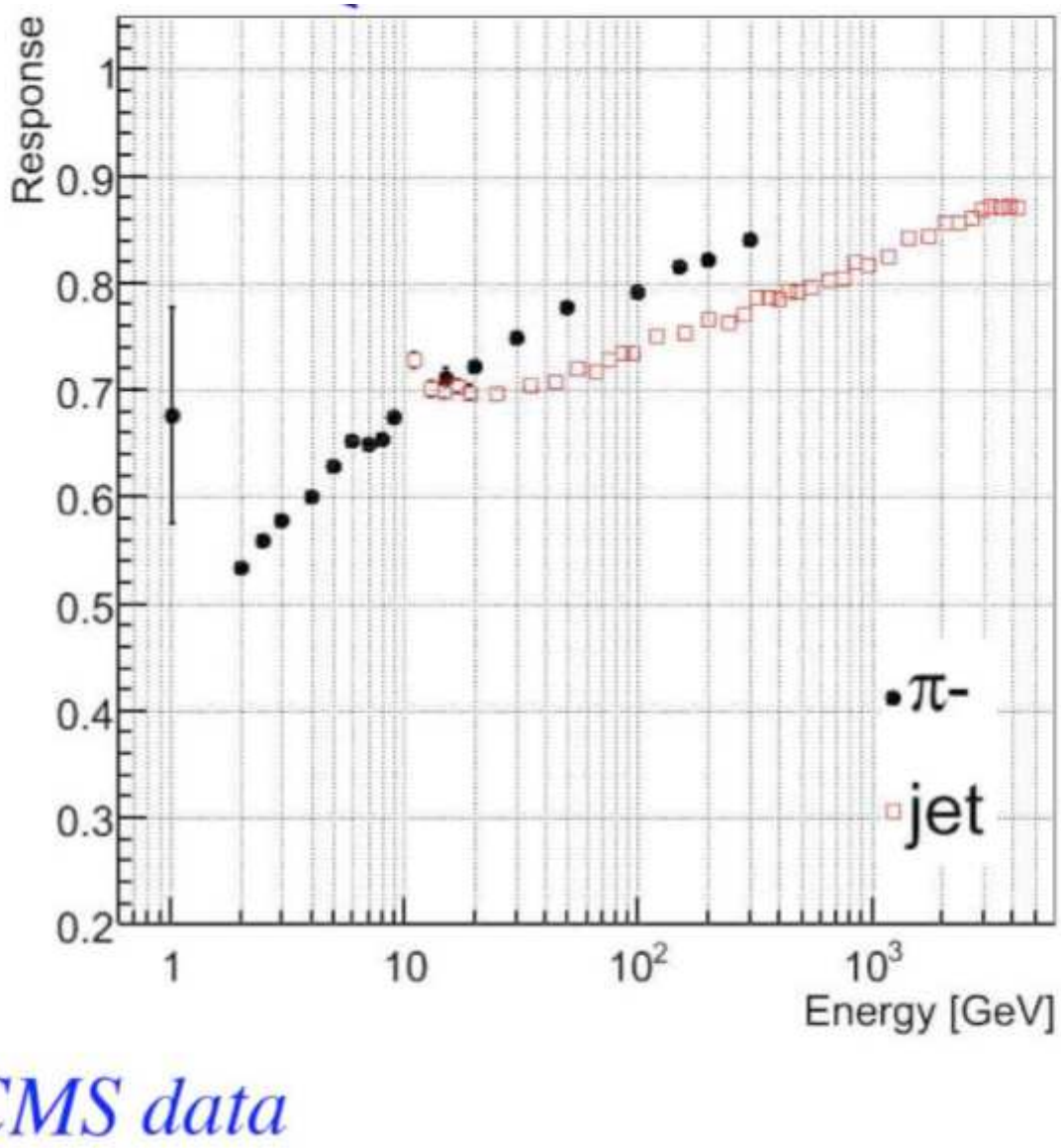

Figure 4: The pion response and the jet response of the CMS hadronic calorimeter.

It makes no sense whatsoever to apply a simple formula involving (e/h) to a low energy proton that is slowing down and stopping within the calorimeter.

It is clear that dual-readout (the measurement of the EM fraction in each shower) largely solves the energy dependence problem. Even a slow proton (that produces zero Čerenkov light) will have a more constant energy response than in any other (single-readout and non-compensating) calorimeter. This is by design. An understanding of the details of EM-fraction fluctuations and the dominant role of spallation protons in hadronic showers that result in measured calorimeter signals leads directly to the dual-readout idea. The DREAM tests have made this clear down to 20 GeV beam energy (Fig. 1) and the 4th simulations makes this clear down to 1 GeV. This simulated response of the BGO+fiber calorimeters to single pions is shown in Fig. 5, showing a 6.5% drop in response to a π^- from 20 GeV down to 1 GeV. This is negligible within a jet.

There is negligible momentum dependence to the response of low energy particles in a dual-readout calorimeter. This is demonstrated in DREAM data down to 20 GeV beam energy, and down to 1 GeV in the FLUKA-ILCroot simulations.

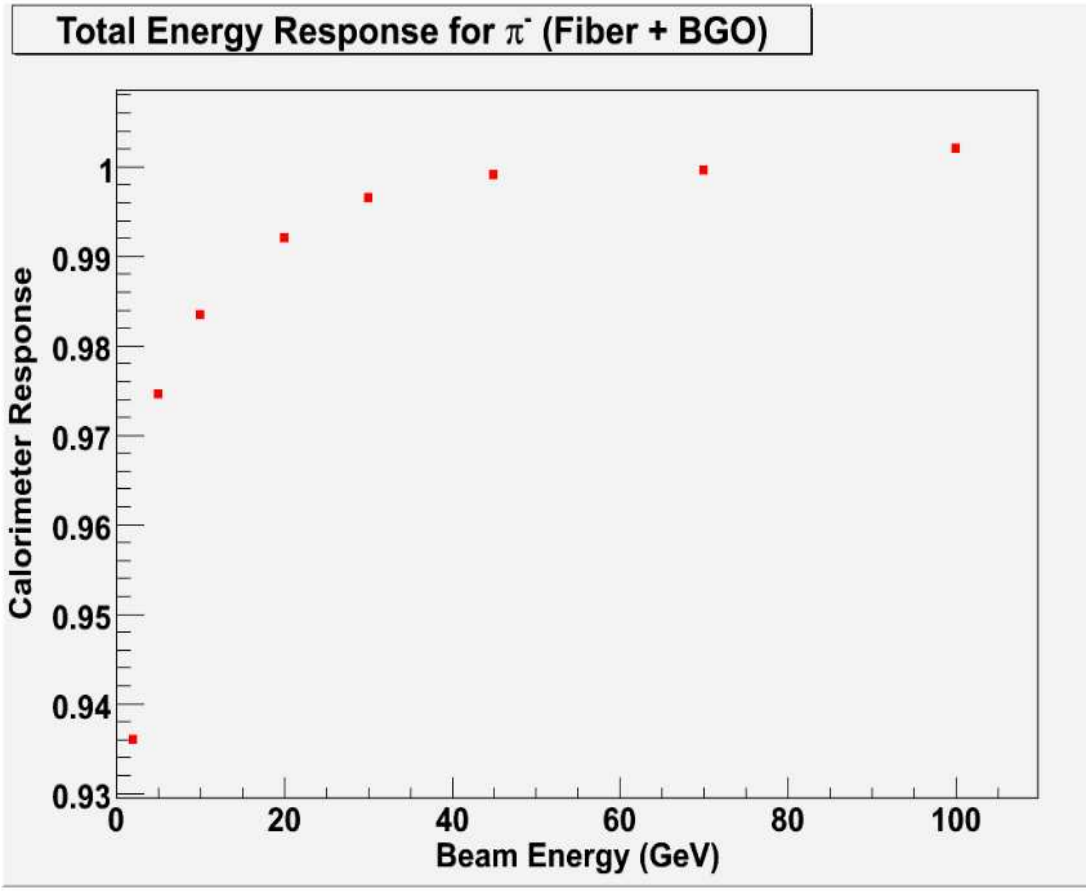

Figure 5: Pion response linearity test from ILCroot simulation (using GEANT4 and FLUKA codes).

3 Post-Tsukuba IDAG Questions (all concepts) (April 20, 2009)

3.1 Plan for calibrating the energy response

Give an outline of the plan for calibrating the energy response of your calorimeter, both from test beams or monitoring signals and in situ running. What level of precision is required? How is it obtained ? How do you monitor and maintain it? If operation at the Z pole is part of your strategy, how much data are required?

- Firstly, the dual-readout calorimeters exist as actually tested calorimeters, we have easily and successfully calibrated them with actual particles, and the results are published.
- Secondly, the directly measured energy resolution is the best achieved of any proposed ILC calorimeter and bottoms out at about 4% limited only by the small size of the test module, as seen in Fig. 48 of the 4th LoI. This raw energy resolution enters the problem of calibration as a *square* and, in the presence of background, as a *cube*.

The time scale for re-calibration will (probably) depend on the electronics and not the physical module, since our experience in the test beam (and common experience) is that fibers are relatively inert, and even the BGO crystals are inert enough, so that drifts are neither large nor fast. We discuss the worst case here in which a full-detector calibration is done with particles of known energies, for example, from Z^0 decays. An electronics-only calibration would be easy and swift by comparison. To illustrate directly the calibration of 4th, we show in Fig. 6 response of the BGO signals for scintillation and Cerenkov to 45 GeV $e^{\pm}$ from $Z^0 \to e^+e^-$ decay.

The hadronic response of the fiber module is shown in Fig. 7 for the scintillation and Cerenkov responses separately, and the dual-readout response.

These are the distributions that would be collected and used in the calorimeter calibration.

A 1% precision on the mean of a Gaussian distribution with N entries is $(\sigma_E/\sqrt{N})/E$. The number of particles per Z^0 is usually 2; the branching ratio of the Z^0 to the desired particle is B, and the number of calorimeter channels to be calibrated is $N_{\rm chan}$. So the number of Z^0 decays required is

$$N_Z \approx [(0.01)^{-1} \cdot (\sigma_E/E)]^2 \cdot (\frac{1}{2 \text{ per } Z^0}) \cdot \frac{1}{B} \cdot N_{\rm chan}$$

These numbers of required Z^0's are shown in the Table below for calibration of the BGO and fiber calorimeters with particles in the colliding beams.

The BGO calorimeter is calibrated in two ways: directly with electrons from $Z^0 \to e^+e^-$, and also by $\pi^0 \to \gamma\gamma$ with a mass constraint. The BGO crystals would be calibrated identically the same way as in the CERN test beam in the first case. The second case benefits from a far larger number of γ's from π^0 than e's from Z^0 decays, but suffers from the problem of correctly pairing γs into π^0s. In the table, the number of Z^0 decays required for 1% calibration precision is 20M Z^0s, or 100 times that for a 0.1% calibration. A calibration using $\pi^0\gamma\gamma$ decays required only 0.2M Z^0 decays.

The fiber calorimeter will be calibrated by two particles: jets from $Z \to jj$ decay (requiring 0.008 Giga-Z) and by $Z \to \tau\tau$, with one tau decaying to pion+neutrino (requiring 0.5 Giga-Z). With reference to Fig. 47 of the LoI, we introduced a conservative factor of 10 in the number

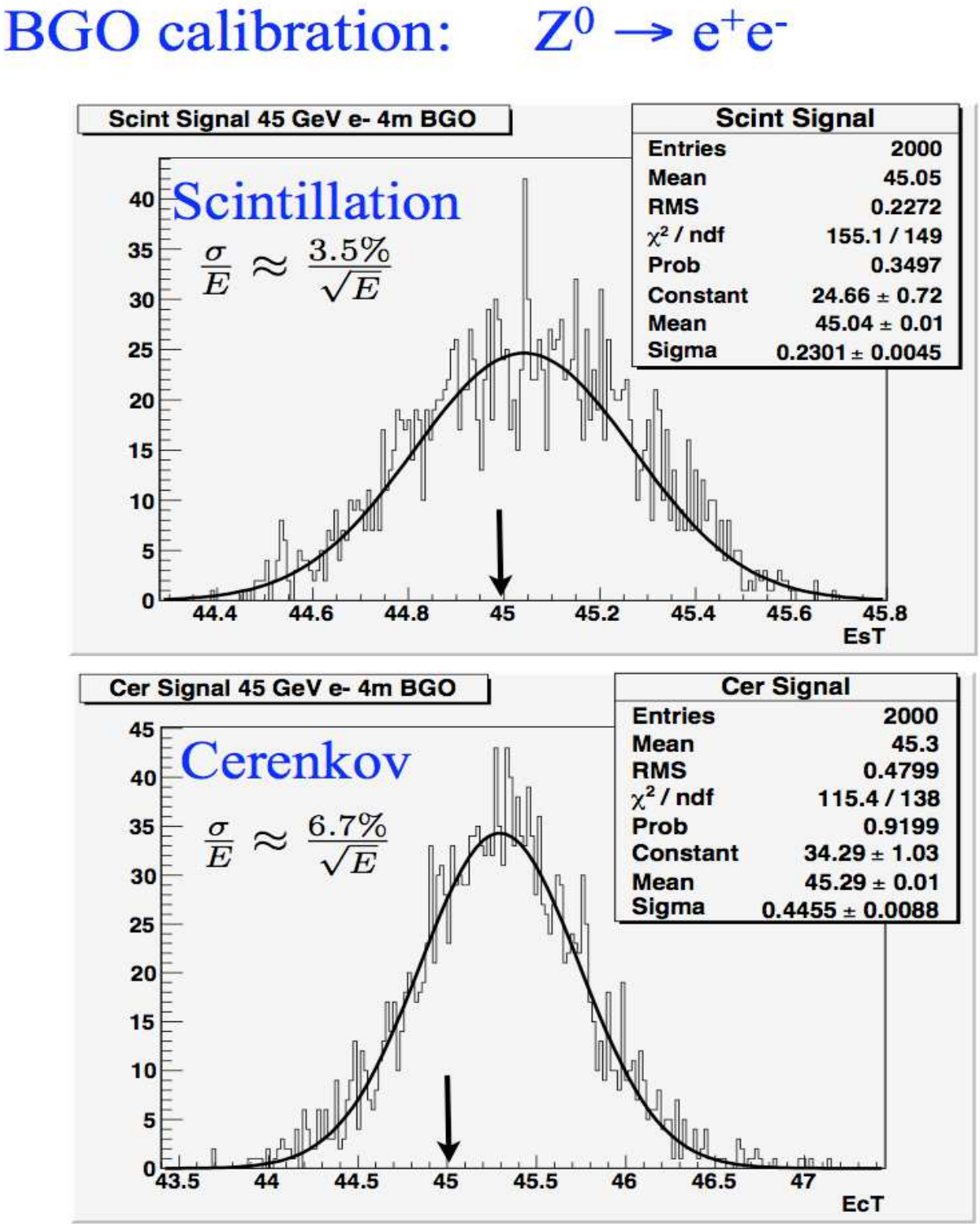

Figure 6: Scintillation and Cerenkov response to electrons from $Z^0 \rightarrow e^+e^-$ decays that would be used for calibration of the crystal BGO calorimeter.

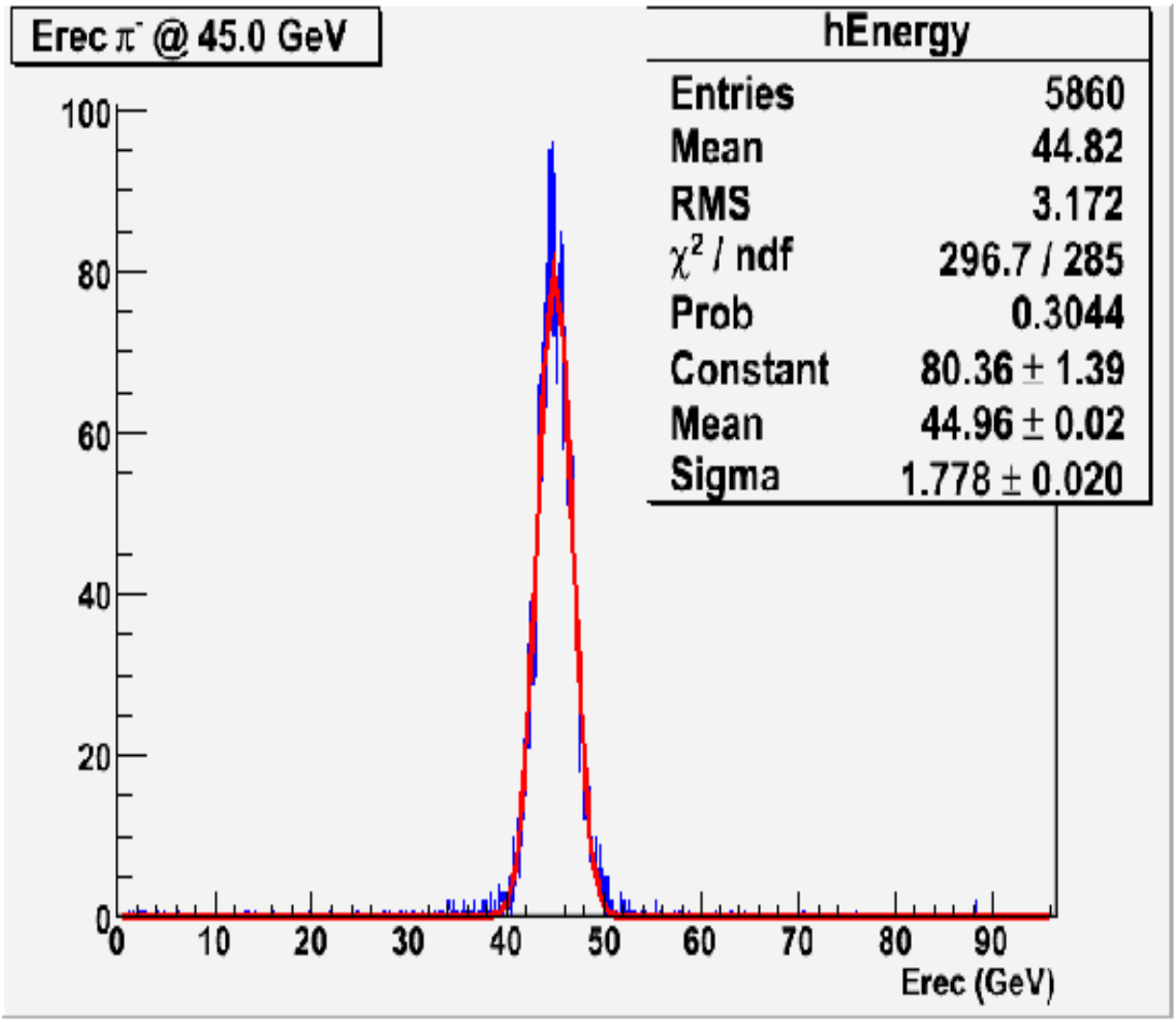

Figure 7: Dual-readout response to 45 GeV π^- in the 4th simulation. This is the resolution that would be used for $Z^0 \to jj$ calibration of the fiber calorimeter.

of $Z \to jj$ events required to account for the lower energy deposit on the average in the fiber calorimeter for jets. For the $Z \to \tau \to \pi$ sample, we introduced a factor of 2 since 1/2 of the pions do not interact in the BGO and they are unambiguously useful for calibration. The other half of the pions is also useful since the dual-readout BGO crystals are higher precision, any energy loss in the BGO is well-measured.

Calor.	part.	σ/μ	σ_E/E (LoI Fig.)	part. per Z	B	$N_{\rm chan}$	$\#Z^0$'s requ'd
BGO	e^-	1% 0.1%	3.5% (Fig. 49)	2	0.03	10^5	$20 \cdot 10^6$ $2000 \cdot 10^6$
BGO	jet$\rightarrow \pi^0$ $\pi^0 \rightarrow \gamma\gamma$	1% 0.1%	3.5% (Fig. 49)	8	0.60	10^5	$0.2 \cdot 10^6$ $20 \cdot 10^6$
fiber	jets	1%	7.0% (Fig. 45)	2	0.60	$2 \cdot 10^4$	$1 \cdot 10^6$
fiber	$\tau^\pm \rightarrow \pi^\pm$	1%	6.0% (Fig. 50)	1	0.03×0.11	$2 \cdot 10^4$	$250 \cdot 10^6$

The most important factor is that the number of required Z^0s goes like $(\sigma_E/E)^2$, so that the exceptional energy resolution of the dual-readout calorimeters *without non-Gaussian tails* works twice. For those final states where background rejection is required to isolate a calibration sample, the energy resolution is used again and, therefore, the calibration ensemble size required goes like $(\sigma_e/E)^3$ (roughly). This is very, very important.

Equally important is the Gaussian response of the dual-readout calorimeters, and the absence of low-side and high-side tails. All of these features allow faster, easier and more robust calibrations. Anybody who has calibrated a calorimeter knows these things.

Response of low energy particles: The DREAM module was calibrated with 40 GeV electrons (or 50 GeV in later tests) once, and only once. This GeV/ADC for each channel was used throughout all studies of pions, muons, and jets at all energies (down to 20 GeV; very low flux below this energy). We have not encountered a problem. We have used the ILCroot simulation to calculate down to 1 GeV where we find a 6% drop in the pion response. This is not critical.

One must recall that for a calorimeter, a low energy particle is a low energy particle, and if its response is unknown to 20%, that is 20% of a small energy.

Species dependent response: As far as species dependent responses, this is answered by the plot on the next page showing response of the CMS calorimeter to $e, \pi, \mu, K, p, \bar{p}$ as a function of the **available** energy. All species lie on top of each other, at least as well as is required for low energy particles in jets.

3.2 Plan for aligning your tracking systems?

What is your plan for aligning your tracking systems?

There are two alignment issues to be considered:

- the alignment between the CluCou chamber geometry and the physics coordinate system; and,
- the alignment between CluCou and VXD.

For the first issue, starting from an accurate surveyed geometrical parameterization of the drift chamber (this can be done with overall tolerances of better than 100 μm, with respect to fiducial marks placed on the chamber structure), there are two kinds of misalignments to take into account:

- global offsets and twists; and,
- wire-by-wire displacements, which include, besides the tolerances on the wire positions at the end plates, also the non uniformities in the gravitational wire sagging (the electrostatic wire sagging has been calculated to be negligible for the CluCou cell configuration).

In principle, for a rigid system like CluCou, the global offsets and twists can be described by the three spatial coordinates of its center and by the three Euler angles. The alignment is obtained by fitting a set of selected gold plated high momentum tracks and by minimizing their residue distributions as a function of these parameters.

At 10^{34} cm^{-2} s-1 luminosity, one expects, for example, of the order of 5000 muons per week from $e^+e^- \rightarrow \mu^+\mu^-$ with $p_T \geq 10$ GeV/c. A comparable number of Bhabha pairs at large angles is expected in the θ angular range from 45 to 135 degs. These events are largely sufficient to determine the global alignment parameters with the required precision.

Obviously, in case of dedicated runs at the Z-pole for energy calibration reasons, the same task will be accomplished in a much shorter time.

The wire-by-wire displacements can be corrected only by using a large statistics sample of fitted tracks. With the order of few hundred thousand tracks, one can individually align each single wire by its coordinates on the end plates and its downward pointing gravitational sag (5 parameters) with a precision of about 20 μm, or better. These data can be collected in a long run period of several months, since these parameters are supposed to be stable with time.

The issue on the relative alignment of CluCou with the VXD can be accomplished only by rigidly constraining the VXD support structure to the inner cylinder of CluCou. In this case, the same sample of events can be used for this purpose.

What is the precision required?

At the level of 20 μm, or better.

Are there special operations needed for alignment after push-pull prior to data taking, and what time is required?

A necessary check of the stability of the mechanical wire tensions must be performed after push-pull operations and prior to data taking. This can be accomplished by inducing mechanical oscillations on the sense wires by means of supplying to them an alternating HV (of the order of 1 kV) with respect to the surrounding field wires and detecting the resonance frequency by the measurement of the variation of the sense wire capacitance with respect to the surrounding field wires. Precisions of the order of 1% on the gravitational sagging of the sense wires can be obtained with this method. The procedure can be made automatic and may require only a few hours to be applied to all sense wires of CluCou. A further operation to be made after a push-pull is the check of the alignment of the CluCou chamber axis with the inner solenoid field axis. This is similar to solving the problem of the global chamber alignment with the physics coordinate system.

How many degrees of freedom need to be considered after a move?

Only six to realign the chamber to the physics coordinate system and, eventually, to the inner solenoid axis.

How do the alignment needs affect the design of your detector?

No particular constraint due to alignment on the chamber design.

Is any real-time monitoring of the tracker alignment envisioned (e.g., related to power pulsing and long term stability)?

No particular monitoring of the tracker alignment except for the usual gas, gain and environmental parameters which affect the time-to-distance relationship and, therefore, might simulate misalignment related problems.

3.3 Repeat the recoil analysis with $Z \to \mu^+\mu^-, e^+e^-$

Repeat the recoil analysis with $Z \to \mu^+\mu^-, e^+e^-$, including the corrected ISR spectrum, and simulation of beam-background hits.

3.3.1 $e^+e^- \to H^0Z^0 \to H^0\mu^+\mu^-, e^+e^-$

(G. Tassielli, giovanni.tassielli@le.infn.it) The methods are the same as described in the LoI, and we solve the problem for three cases ($\mu^+\mu^-, e^+e^-$ with tracking only, and e^+e^- with tracking and calorimetry) with the resulting missing mass distribution shown in the indicated Figure.

$$e^+e^- \to H^0Z^0 \to H^0\mu^+\mu^- \quad \text{(Fig. 8)}$$

$$e^+e^- \to H^0Z^0 \to H^0e^+e^- \quad \text{(Using tracking only : Fig. 9)}$$

$$e^+e^- \to H^0Z^0 \to H^0e^+e^- \quad \text{(Using tracking + calorimetry : Fig. 10)}$$

Integrating the fitted functions in these plots yields the cross section estimates in the Table, in which the selection efficiencies are also quoted. The mass resolution on the Higgs (for a simulated mass of 120 GeV/c^2) from a fit to signal + background is shown in the last column:

Event sample	expected cross section	meas'd cross section	uncertainty on cross section	selection efficiency	Figure number	fitted Higgs mass (GeV/c^2)
$Z^0 \to \mu^+\mu^-$	11.664 fb	8.952 fb	$\pm$ 0.907 fb	71.8%	Fig. 8	120.28 ± 0.68
$Z^0 \to e^+e^-$ tracking only	12.532 fb	13.472 fb	$\pm$ 1.748 fb	67.2%	Fig. 9	120.49 ± 0.85
$Z^0 \to e^+e^-$ tracking + calorimeter	12.532 fb	10.884 fb	$\pm$ 1.594 fb	70.9%	Fig. 10	120.15 ± 0.76

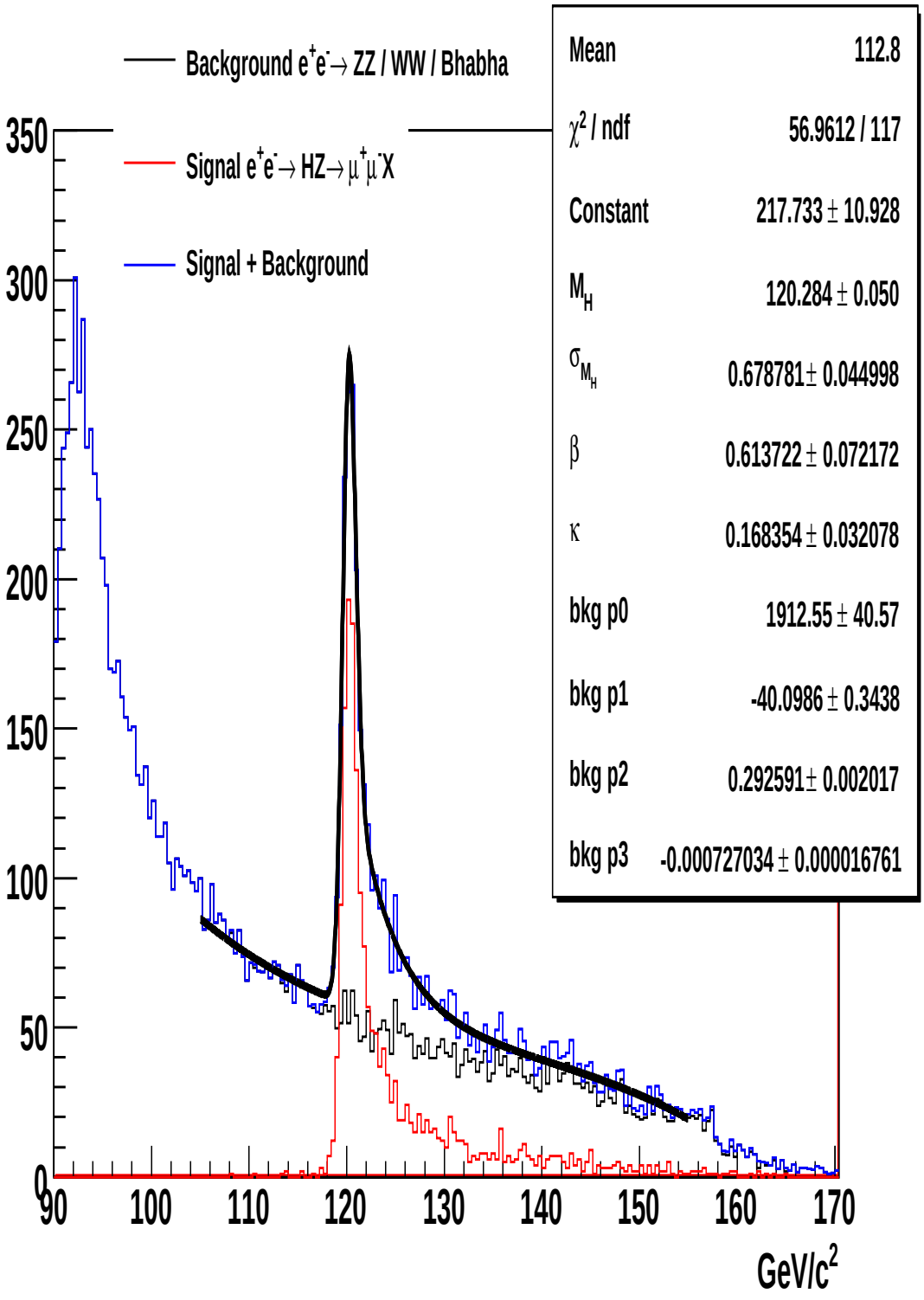

Figure 8: Missing mass distribution against the $Z^0 \rightarrow \mu^+\mu^-$ system for the process $H^0Z^0 \rightarrow H^0e^+e^-$.

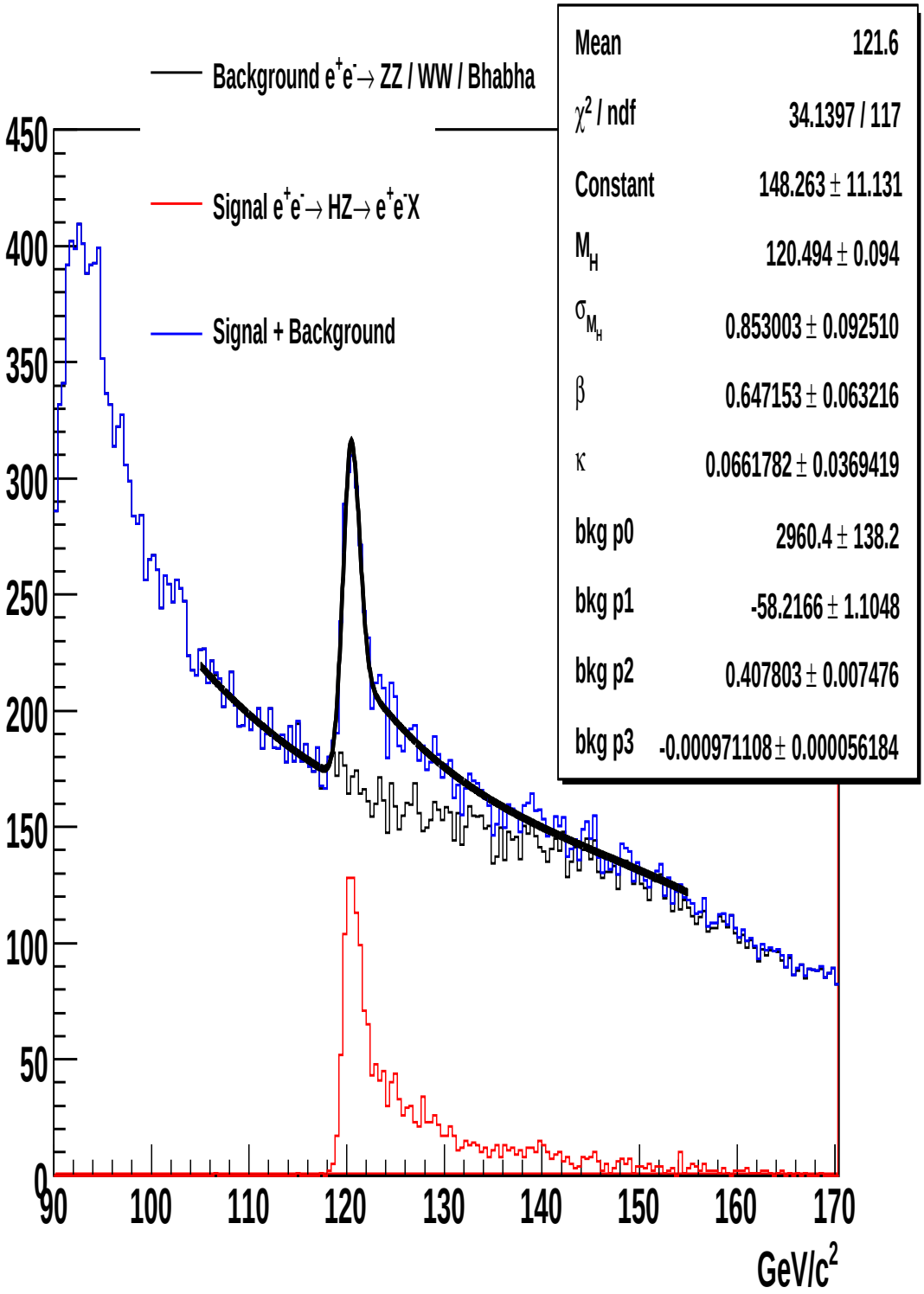

Figure 9: Missing mass distribution against the $Z^0 \to e^+e^-$ system for the process $H^0Z^0 \to H^0e^+e^-$ using only the tracking system information on the electrons.

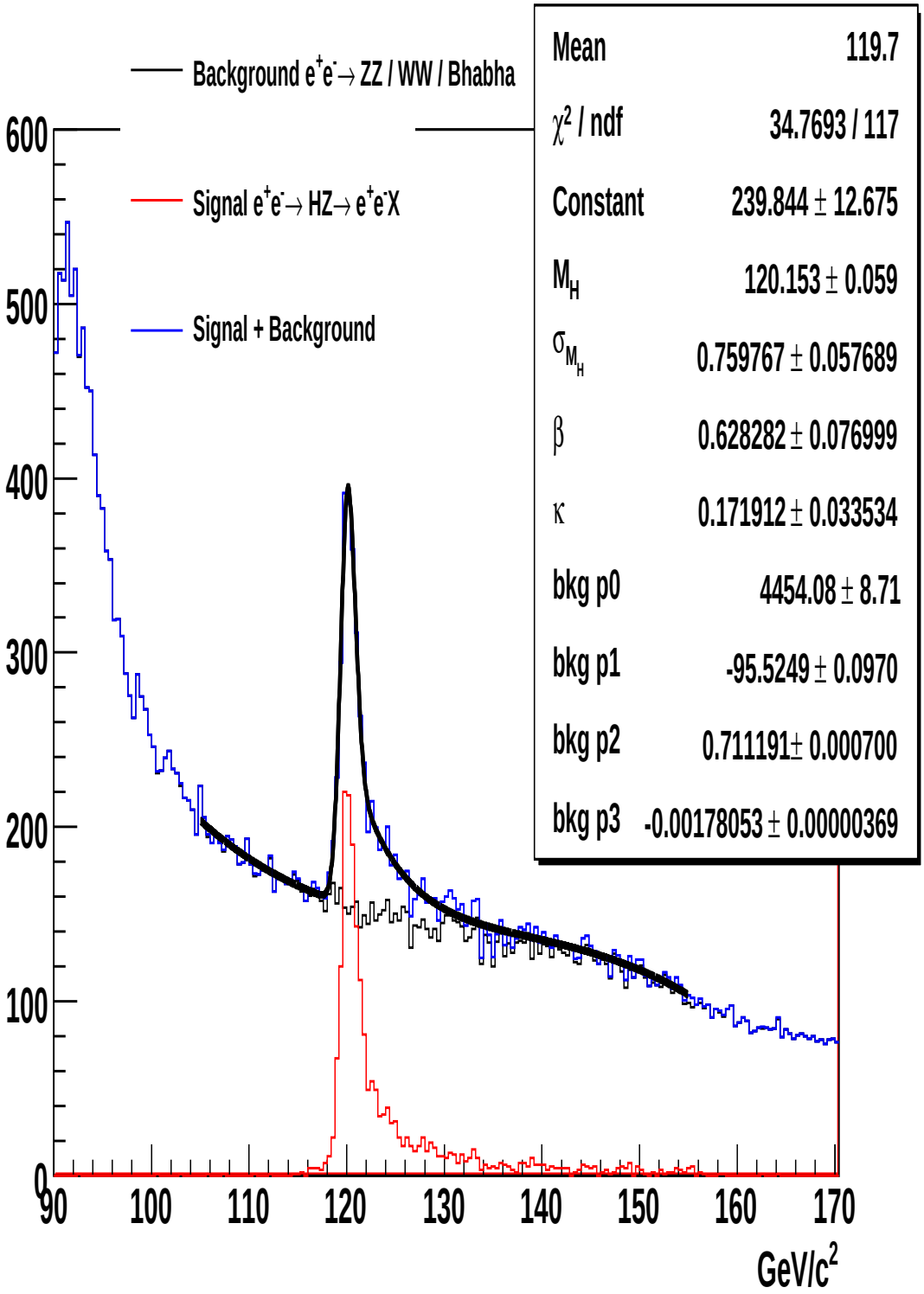

Figure 10: Missing mass distribution against the $Z^0 \rightarrow e^+e^-$ system for the process $H^0Z^0 \rightarrow H^0e^+e^-$ using the tracking system and the calorimeter systems for the electron measurements.

4 Post-Tsukuba IDAG Questions (4th) (April 20, 2009)

4.1 We would like to see a more complete description of your baseline detector

We would like to see a more complete description of your baseline detector for:

(a) The photodetectors for the BGO and fiber calorimeter We know that we can use "silicon PMs" (SiPM). Mikhail Danilov has given talks (LCWS08, TILC09) on the use of thousands of SiPMs in the CALICE tests. On 4th, our demands are slightly larger:

- we want absolute linearity, without Geiger pixel saturation;
- we want lower dark current rates (maybe ameliorated by cooling);
- we want no "after pulsing", which would mask the neutron signal; and,
- we want faster recovery time between pixel firings in the forward calorimeter towers to avoid saturation effects at high event rates.

This is all a tall bill. Danilov has suggested some solutions, such as a high impedance on each pixel, and there may be more ameliorations. We will study all options, especially since the rate of improvement in SiPMs is still large. This item is on our R&D list for LCRD funding to DoE-NSF.

We also know the CMS solution for photo-converters, and its upgrade to SiPMs.

We also know that micro-channel plate (MCP) photo-converters have interesting properties, low sensitivity to B fields, and recent progress has been made on these (see "Photomultiplier tubes with three MCPs", Barnyakov, A., *et al.*, Budker Institute, NIM **A598** (2009) 160).

We know we will have an acceptable physics solution, it is only a question of how much we like it.

(b) The mechanical support system for the calorimeters The calorimeter support was first studied by Zhijing Tang (Fermilab) and his report is included in Appendix A of the LoI (and available on the website www.4thconcept.org): "Conceptual Design of ILC 4th Calorimeter Support", Zhijing Tang, May 2, 2007 (Fermilab note) We include here a representative drawing from his report in Fig. 11. The full report is available in the 4th LoI Appendix C titled "C.Engineering-ZhijingTang-calor-support.doc".

The support of the crystals inside the fiber calorimeter has been studied by Alessandro Miccoli. Alessandro started from the BaBar solution for support of the CsI crystals:

"Technical Design Report for the BaBar Detector," Chapter 7, ("Electromagnetic Calorimeter")

and went beyond this design with current new materials like carbon fiber composites. This support is detailed in the following figures illustrating that the BGO can be supported *without dead regions.*

The fiber calorimeter is deeper and more massive, but can be easily supported (cantilevered) from the four corners at the back of the module where we can safely leave out a small cluster of fibers. This is illustrated in Fig. 17.

(c) The forward tracking system We deliberately have not inserted a forward tracking system into GEANT. It is easy to do and makes benchmark processes look better. But we hold back on this decision for all the reasons given in Sec. 1.8.

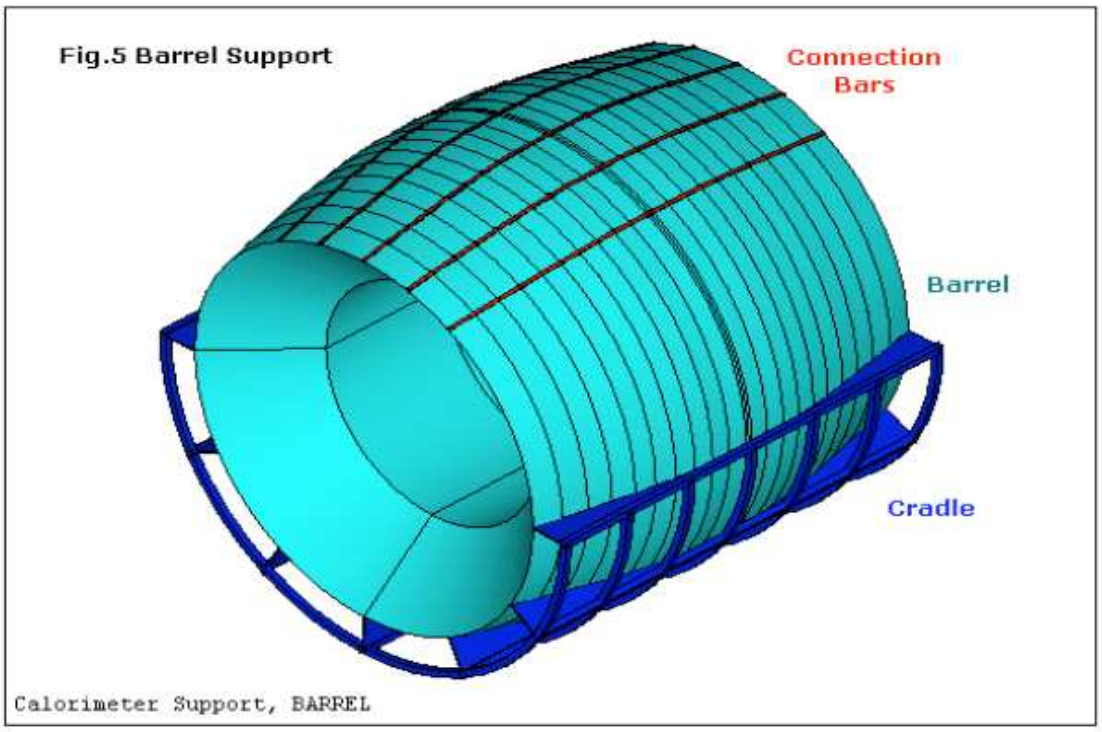

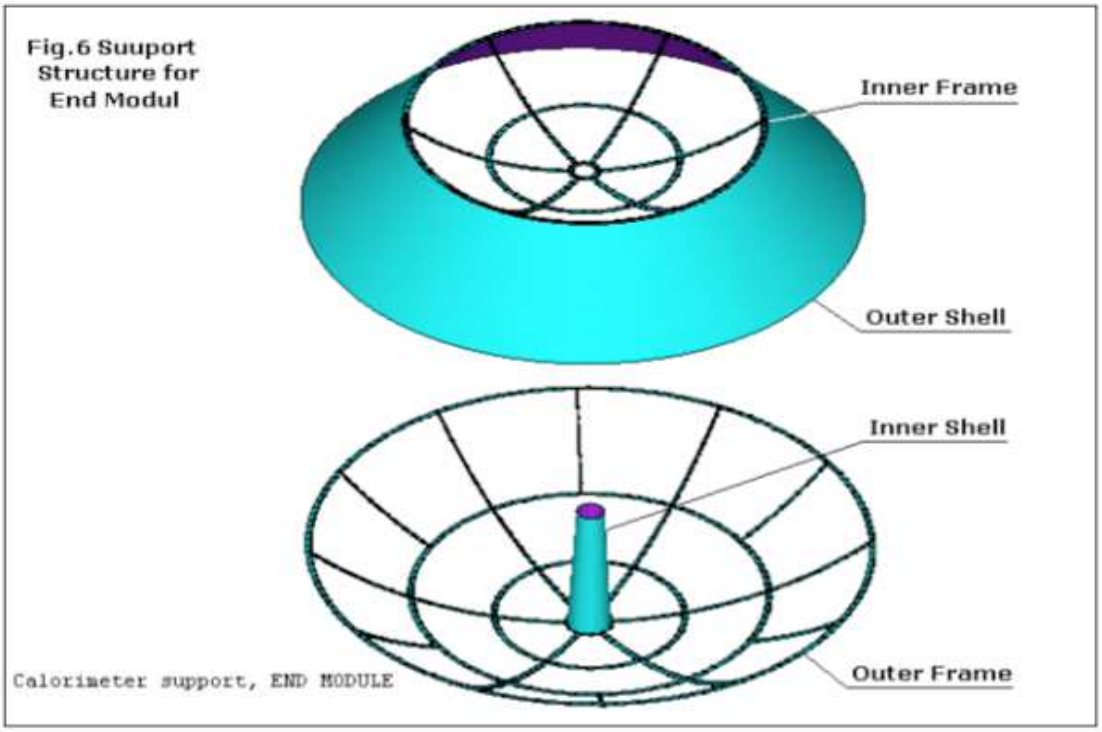

Figure 11: Detail of fiber calorimeter support, Zhijing Tang, Fermilab. The full report on calorimeter support is available in the 4th LoI Appendix C as "C.Engineering-ZhijingTang-calor-support.doc".

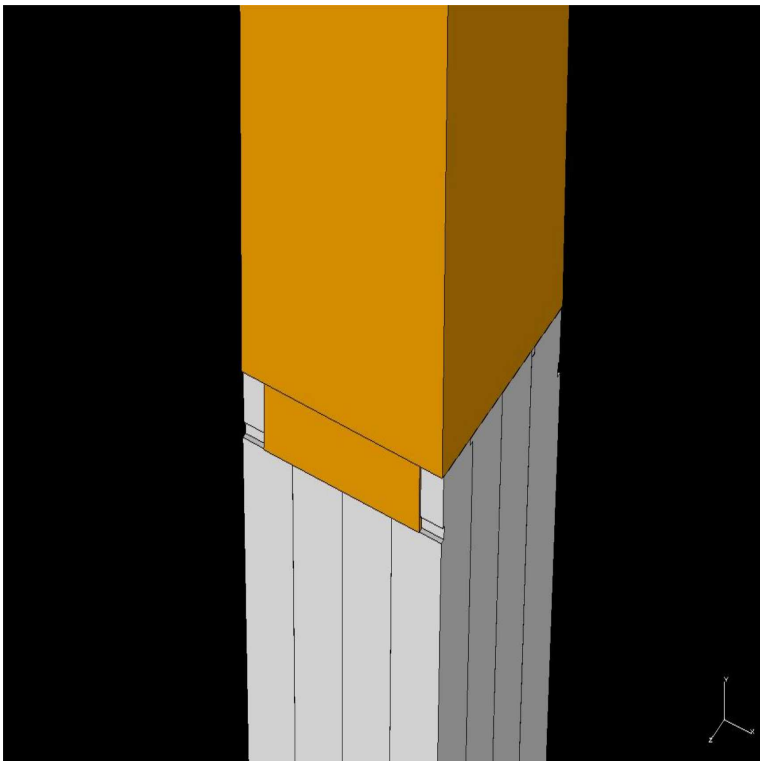

Figure 12: Crystal BGO fixture.

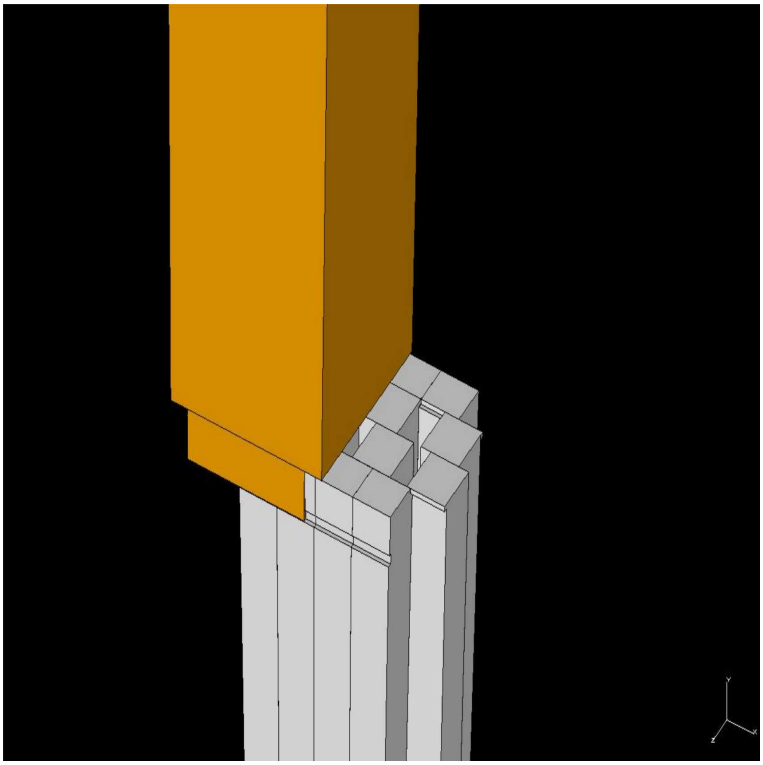

Figure 13: Crystal BGO support.

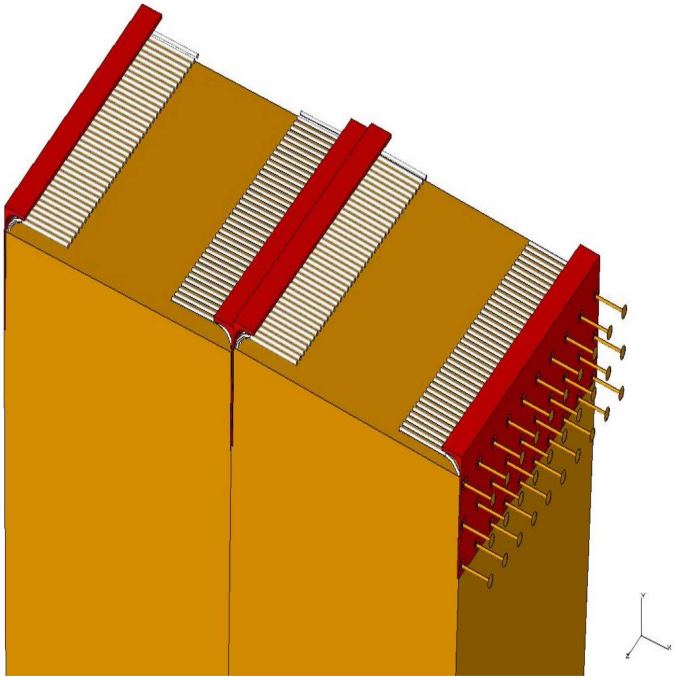

Figure 14: BGO supports.

Figure 15: BGO crystals and mount (photograph).

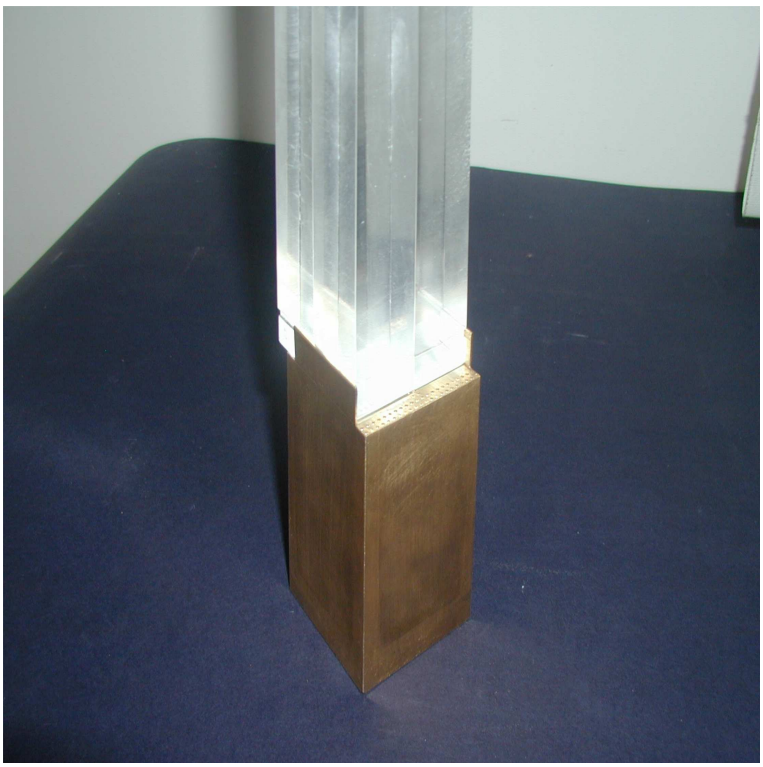

Figure 16: BGO crystals mounted (photograph).

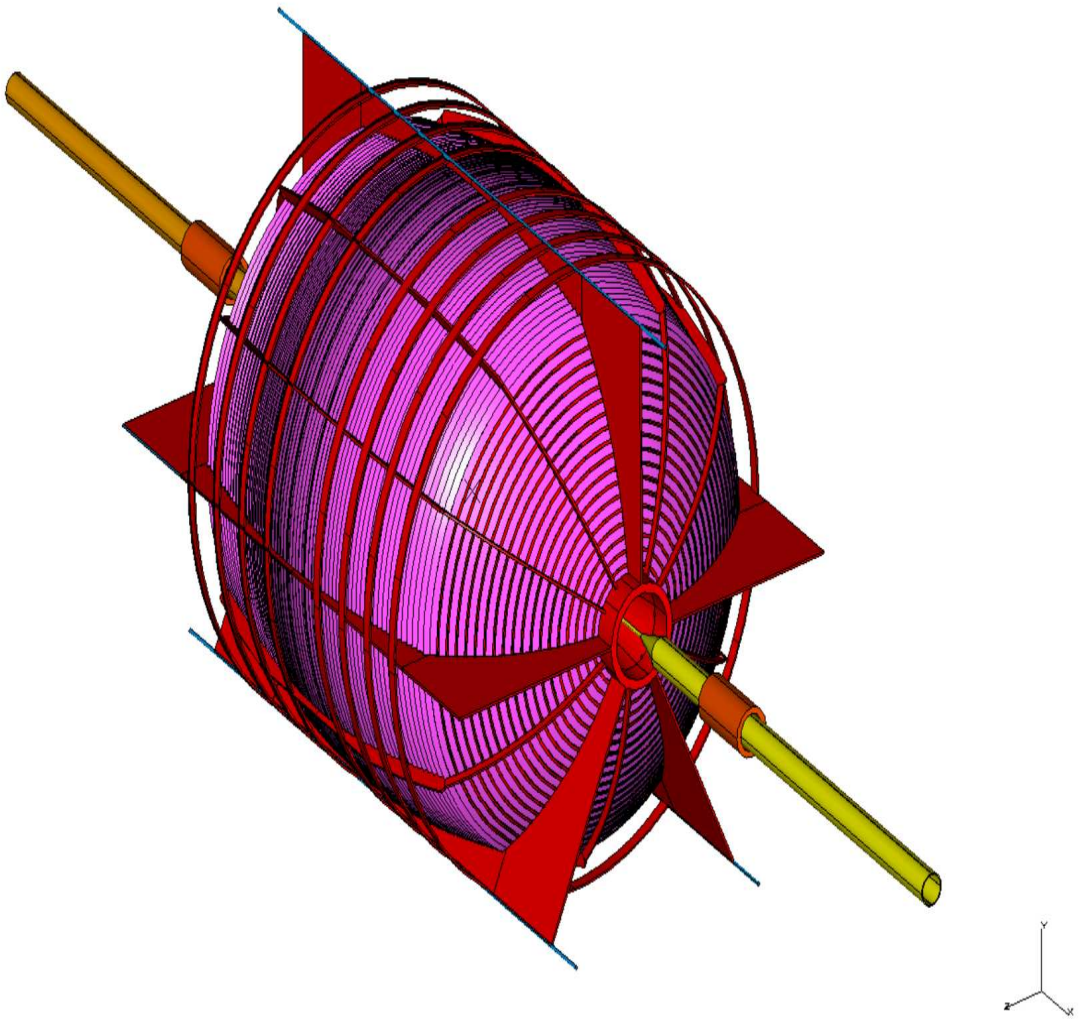

Figure 17: Supports for the fiber calorimeter, showing beam pipe. This structure fits inside the inner solenoid.

4.2 What is the expected tracking efficiency of CluCou?

What is the expected tracking efficiency of CluCou chamber in a 250 GeV jet and background, under the conservative assumption that for multiple occupancy in a cell the hits due to larger impact parameter tracks are lost.

In the 4th LoI we have performed the $t\bar{t}$ production benchmark analysis. In doing so we have assumed, in case of double occupancy in a cell, a resolution of 55 μm for the first hit and 120 μm for the second one (2hits/55μm-120μm).

Since the algorithm for the double-hit separation within a cell presents efficiencies which are strongly dependent from the impact parameters of both tracks, we have now re-analyzed these data, which have the highest track multiplicity, in the conservative assumption that the hits due to larger impact parameter tracks are lost (1hit/55μm). Moreover, just to demonstrate that for such high multiplicities events the momentum resolution is totally dominated by the multiple scattering even in a tracker with extremely low mass, we have re-analyzed these data in the more conservative assumption of 100 μm resolution, instead of 55 μm, and single hit efficiency (1hit/100μm).

In the following table we report the relative efficiencies for reconstructable tracks ($p_T \geq 0.2$ GeV/c, > 10 hits in CluCou or > 4 hits in VXD) in the three configurations.

#hits and resolution(s)	Efficiency for reconstructable tracks	
2 hits at 55μm and 120μm	99.9157 %	0.0017 %
1 hit at 55μm	99.7781 %	0.0027 %
1 hit at 100μm	99.7769 %	0.0027 %

The negligible loss in efficiency, (0.138 0.003)%, once the second hit is dropped, can be attributed to tracks in the very forward direction which have a number of hits close to the limit (10), as shown in the following plot of efficiency versus theta angle.

This efficiency is shown in Fig. 18 as a function of polar angle θ.

These high efficiencies (in simulation) result from the property that CluCou is a continuous tracker (like a TPC) with excellent single point spatial resolution due to the cluster timing, and the Kalman filter used in reconstruction is most powerful in this circumstance.

From the same table we also conclude that there is no difference in efficiency, within the errors, in case of a chamber resolution almost twice as worse (55μm $\rightarrow$ 100μm).

As far as track parameter resolutions are concerned, in the following plot are shown the fits to the distributions in the three mentioned cases. The only appreciable difference is, obviously, in the momentum resolution at high momenta for the case of 1hit/100μm.

A fit to the top invariant mass gives the values reported in the following table.

#hits and resolution	# of initial top sample	# of fitted top events	top mass (GeV/c^2)	top mass resolution
2hits/55μ-120μm	63283	10052.7	174.206 $\pm$ 0.050	4.654
1hit/55μm	62302	9632.6	174.163 $\pm$ 0.060	4.637
1hit/100μm	62329	9625.1	174.159 $\pm$ 0.060	4.651

The small difference in the number of events in the initial sample is due to the fact that some of the data runs crushed during simulation.

From the table it is evident that the top fitted parameters are insensitive of the negligible loss of efficiency due to the very conservative assumption that, in case of multiple cell occupancy, only the first hit be considered.

The total loss of events in the invariant mass top peak is equivalent to less than 0.4% of the initial sample of top events. With a high degree of confidence, we can then state that, due to

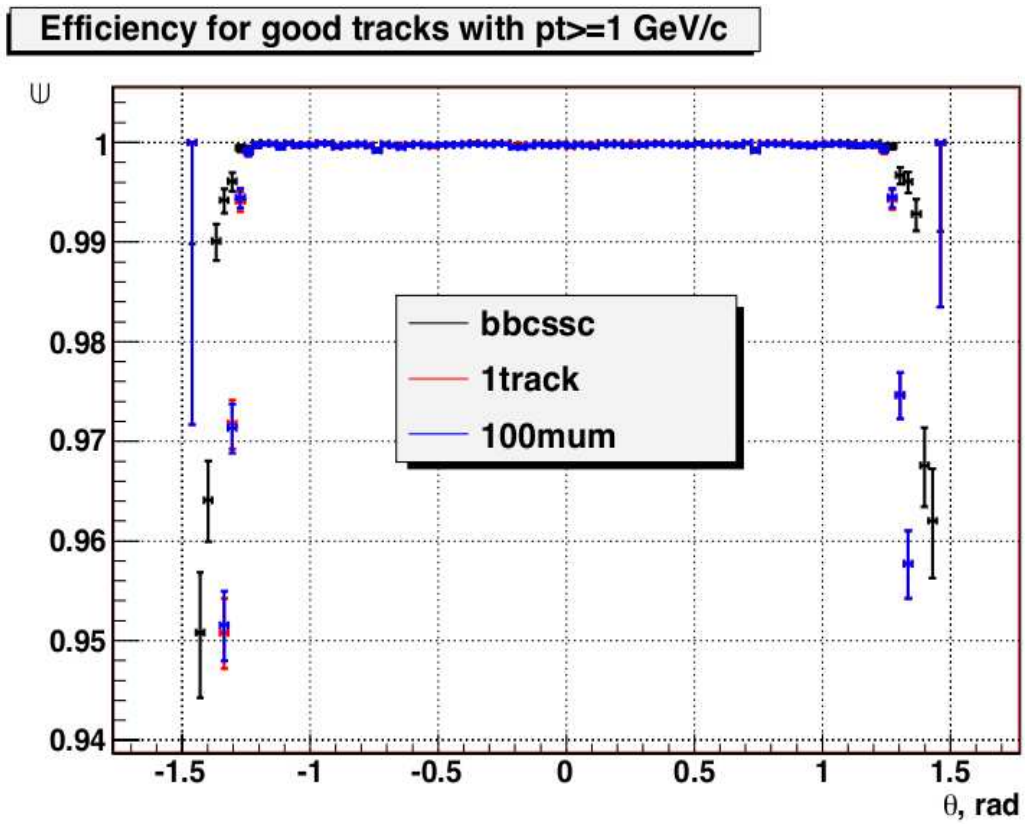

Figure 18: The efficiency of finding 'reconstructible tracks" with the Kalman filter in CluCou.

the very large redundancy of the CluCou tracking detector, in case of multiple cell occupancy, the assumption of totally neglecting the hits at larger impact parameters affect in an almost negligible way the tracking efficiency and has no relevance whatsoever on the track resolutions.

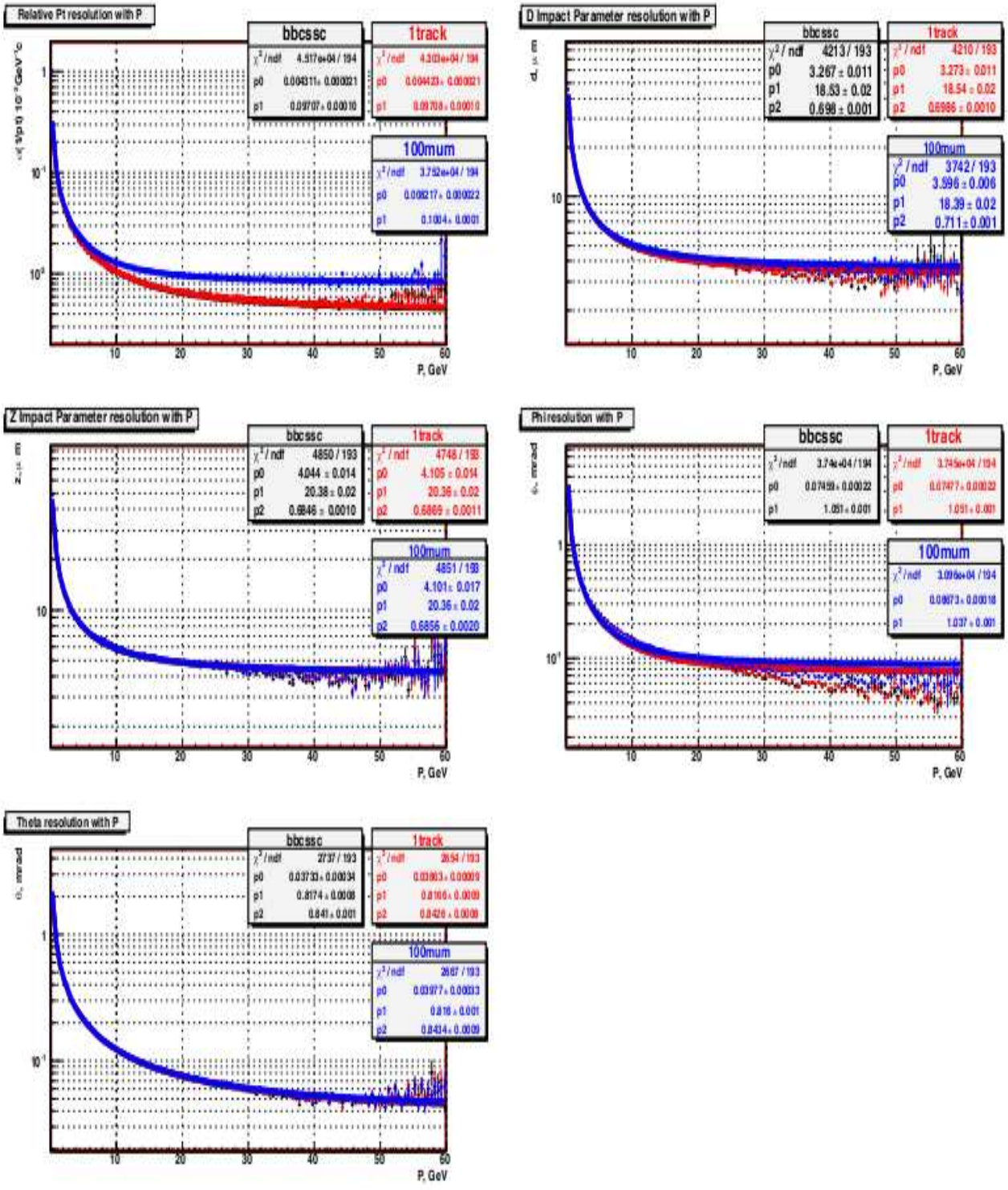

Figure 19: CluCou resolutions for all five track parameters as a function of p_T.

4.3 Perform the Chargino/Neutralino benchmark analysis

Perform the Chargino/Neutralino benchmark analysis including

(i) all background processes,

(ii) beamstrahlung and bremsstrahlung,

(iii) polarized beams ($P_{e^-} = 80\%, P_{e^+} = 30\%$), and

(iv) all detector subsystems. The most important aspect in this is the analysis of background from charginos in the neutralino analysis and vice versa.

4.3.1 $e^+e^- \to \chi_1^+\chi_1^-/\chi_2^0\chi_2^0, \quad \sqrt{s} = 500$ GeV

(A. Mazzacane, Anna.Mazzacane@le.infn.it)

In order to measure the masses of charginos and neutralinos which are important parameters in Supersymmetry, we studied the chargino and neutrino pair production at $\sqrt{s} = 500$ GeV through the following processes:

$$e^+e^- \to \chi_1^+\chi_1^- \to \chi_1^0\chi_1^0 W^+W^- \quad (1)$$

$$e^+e^- \to \chi_2^0\chi_2^0 \to \chi_1^0\chi_1^0 Z^0Z^0 \quad (2)$$

In this analysis we reconstructed invariant masses of hadronically decaying $W^\pm$ and Z^0 bosons from decays of $\chi_1^\pm$ and χ_2^0, respectively. The signature of both signal processes is thus four jets with large missing energy.

The Monte-Carlo *SUSY* sample used for this study included chargino/neutralino signals and SUSY backgrounds and corresponds to an integrated luminosity of $\sim 207\ fb^{-1}$.

80% electrons left-handed and 30% positrons right-handed polarization of the beams was considered.

To identify events of the all-hadronic channel all reconstructed particles are clustered into four jets. We label the 2-jet combinations as W_1 and W_2, and choose the combination with the minimum value of $|M_{W_1} - M_{W_2}|$. Note that the W or Z masses are *not* used in this procedure, but merely requiring proximity of the two 2-jet masses.

The following selections have been applied:

1. Number of jets = 4;
2. Number of charged tracks > 20;
3. Total visible energy < 250 GeV;
4. No isolated leptons in the jets

The selection efficiency of the chargino channel is $37.3 \pm 0.4\%$, and the selection efficiency of the neutralino channel is $34.6 \pm 0.4\%$

The distribution of the 2-jet masses is shown in Fig. 20 revealing a strong W peak and a weak Z peak. The 2-dimension plot of one 2-jet mass *vs.* the other 2-jet mass is shown in Fig. 21. From the fit in Foig. 20, the mass resolutions on the W and Z are

Gauge boson	Fitted mass (GeV/c^2)
W	79.84 ± 3.03
Z	90.52 ± 2.56

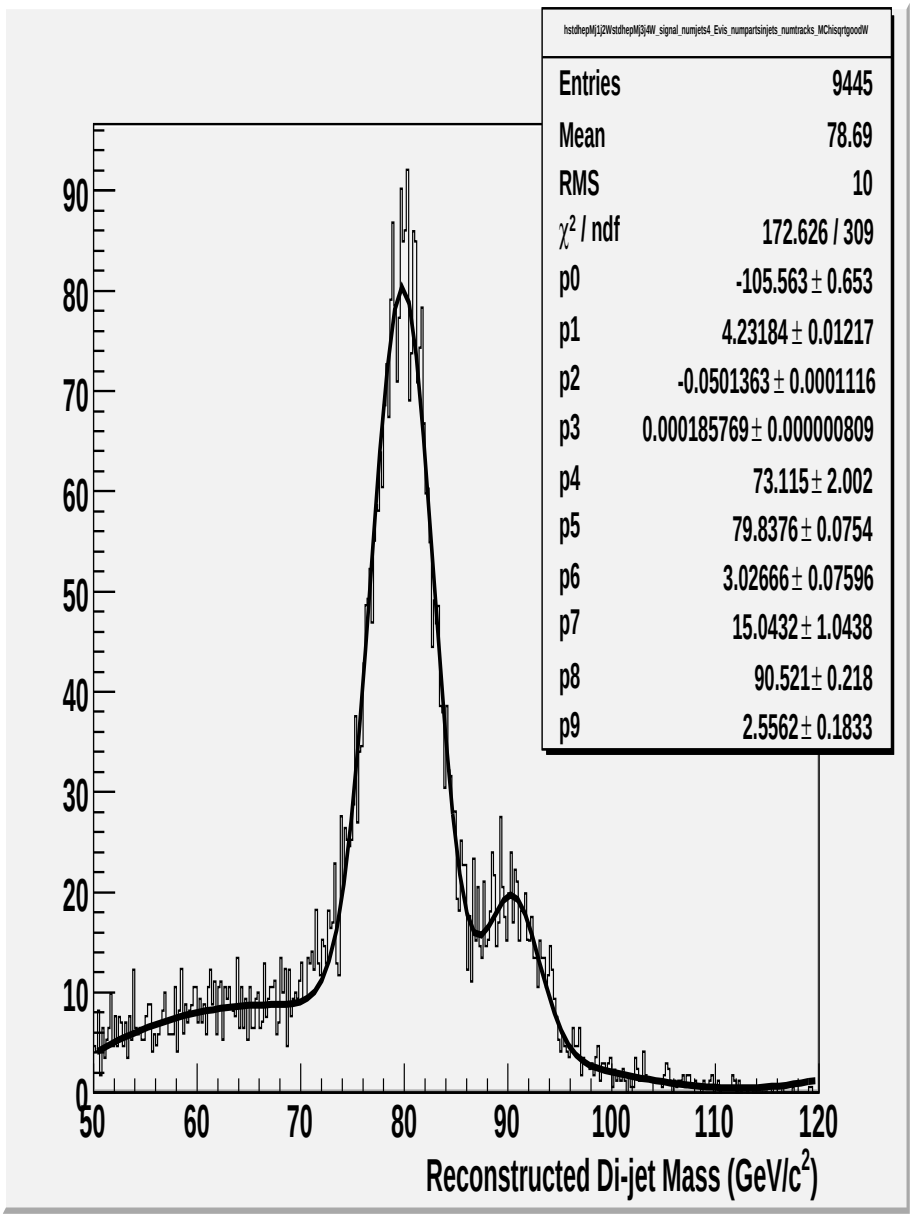

Figure 20: The di-jet mass distribution from raw simulation and jet reconstruction.

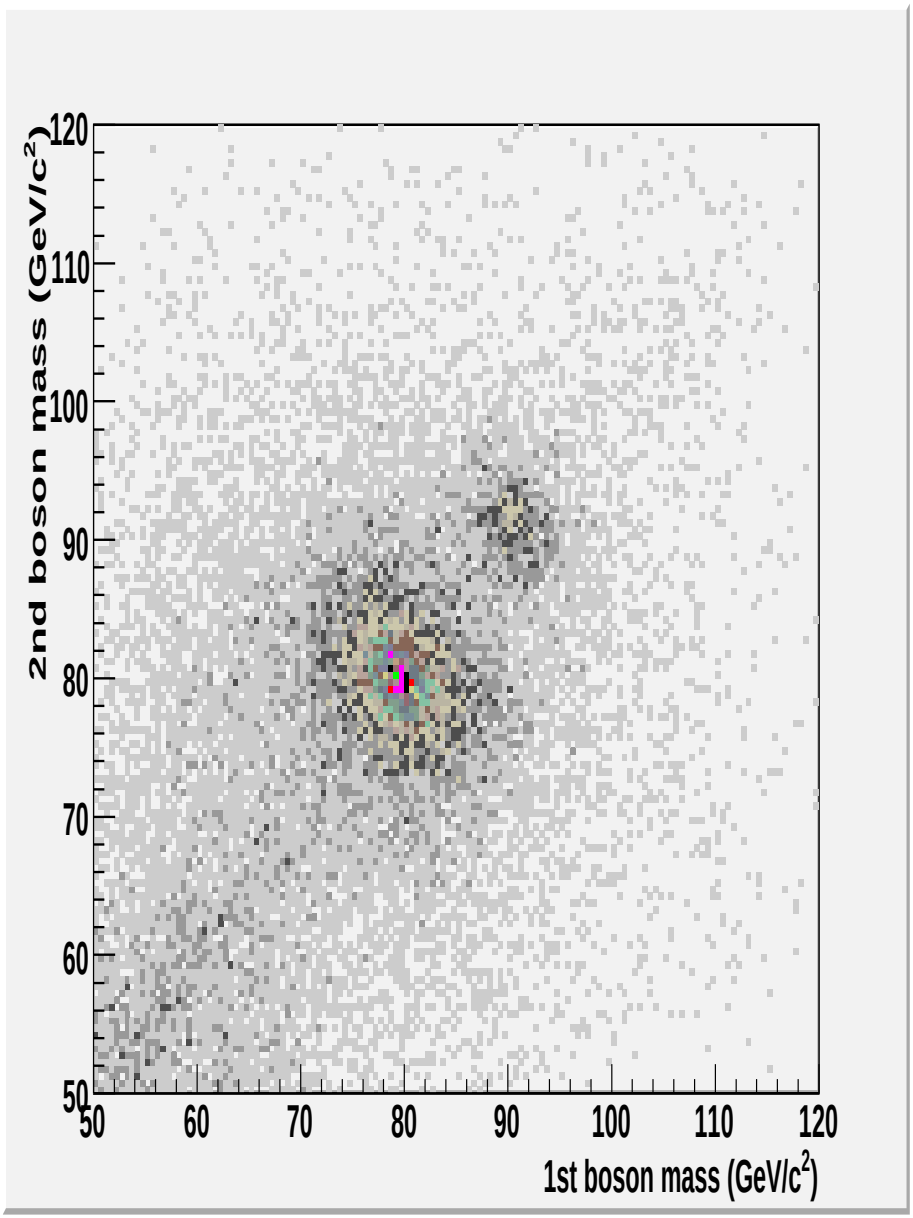

Figure 21: The di-jet mass distributions for two jets out of four jets, plotted $M_{j_1 j_2}$ *vs.* $M_{j_3 j_4}$.

4.4 Comparison of the DREAM data and 4th simulations

Make a proper comparison of the DREAM data and the simulations (with/without BGO) to validate the simulation results.

4.4.1 DREAM data comparisons to 4th simulations "by hand"

For definiteness, we take 200 GeV π^- in both DREAM data (Fig. 22) and 4th ILCroot simulations (Fig. 23). The resolutions are

$$\sigma_E/E = 8.557/204.8 = 4.176\% \qquad \text{(DREAM data, Fig. 22)}$$

and

$$\sigma_E/E = 5.170/197.5 = 2.618\% \qquad \text{(ILCroot 4th simulation, Fig. 23)}$$

The simplest understanding is that this difference results from leakage in DREAM (small 1t test module) that is absent in the 4th simulation (complete 4π detector). Therefore, write

$$(\sigma_E/E)^2_{\rm DREAM} = (\sigma_E/E)^2_{\rm 4th} + (\sigma_E/E)^2_{\rm leakage}$$

or

$$(4.176\%)^2 = (2.618\%)^2 + (3.254\%)^2.$$

This leakage fluctuation of 3.254% due to side leakage is consistent with our guess of 4% leakage (based on lateral shower shapes, "Comparison of High-Energy Hadronic Shower Profiles Measured with Scintillation and Cerenkov Light", *NIM* **A584** (2008) 273, Akchurin, *et al.*, DREAM collaboration) and the reduction in this fluctuation by including the large scintillation leakage counters.

> Therefore, we can easily understand that DREAM data and 4th ILCroot simulations are compatible. There are no large, or even small, inconsistencies.

We should also remark that the essentially raw data in Fig. 22 show the best energy resolution of any proposed ILC calorimeter. There are no comparable data presented to IDAG for comparison. We would like to see a comparable distribution from the data collected in a CALICE calorimeter up to 300 GeV in the CERN H6 beam.

We follow this conclusion with a discussion of leakage measurements in the DREAM module illustrated with data. We actually understand a great deal about this dual-readout module.

The 1 kt DREAM module has leakage fluctuations of about 4%. This leakage is mostly neutrons, and our measurements of this leakage event-by-event with large scintillation counters in the July 2008 beam test show that the neutrons are anti-correlated with the electromagnetic fraction (f_{em}) event-by-event, see Fig. 24, and that about 70 neutrons are seen in the surrounding scintillation counters for a 300 GeV hadronic shower with f_{em}= 0.50. The calibration of the counters was in *mip* units using beam muons and gave an energy calibration of 0.37 GeV/*mip*. Therefore, 70 *mips* is about 26 GeV of energy in neutrons, or about 10% of the shower energy at f_{em}= 0.50. This is all in accord with expectations for hadronic showers.

Furthermore, 70 neutrons is large enough that these leakage fluctuations are Gaussian, and therefore degrade the Gaussian resolution in quadrature, that is, without introducing low-side tails in the calorimeter response. This is a point that CALICE, SiD and ILD people have misunderstood all along in their criticisms of DREAM data. In a thin calorimeter (5.5-6.7 $\lambda_{\rm int}$) leakage fluctuations out the back **will result in low-side tails**, but this is merely a direct consequence of a shallow calorimeter. This is a problem for the many CALICE calorimeters, not for the DREAM module.

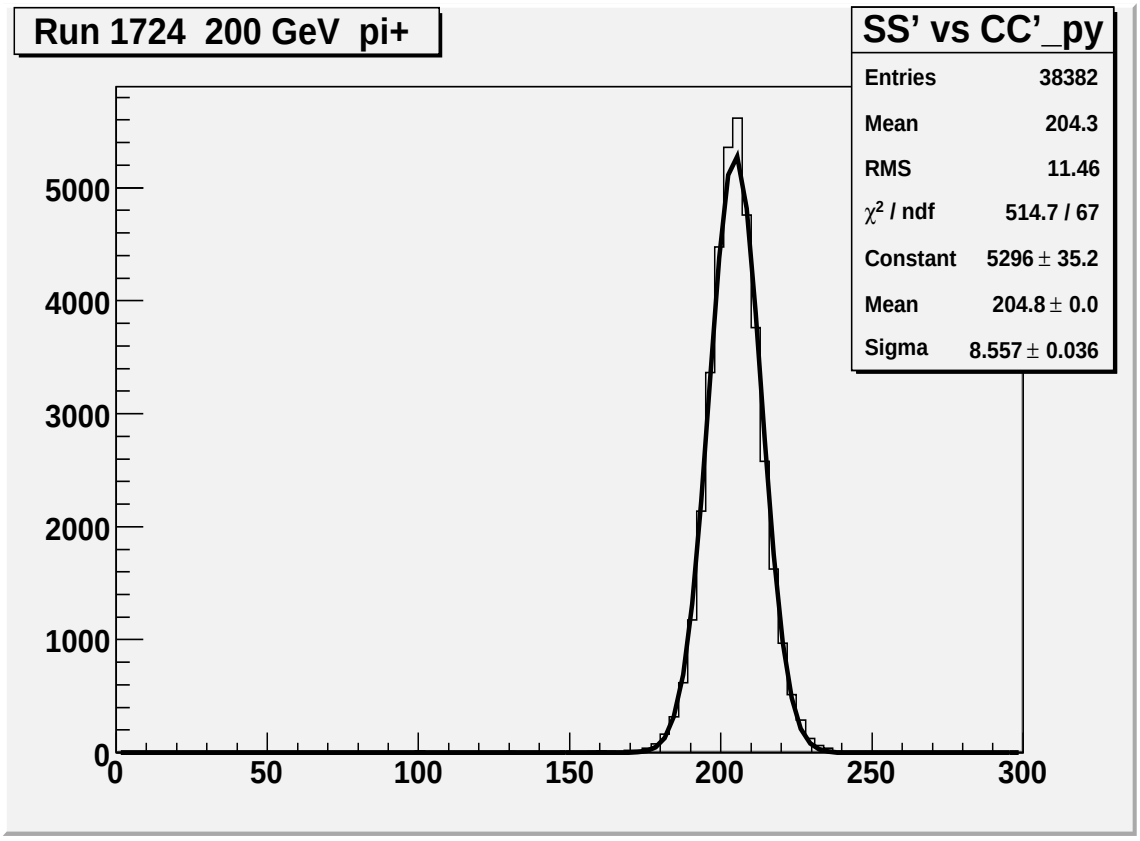

Figure 22: Dual-readout response of the BGO+DREAM module to 200 GeV π^- in CERN H4 beam. This distribution with energy resolution of $\sigma_E/E = 4.2\%$ is essentially raw data from the July 2008 DREAM test.

A direct measure of the energy degradation of DREAM due to neutron leakage is shown in Fig. 25 showing a 15% improvement in energy resolution when the scintillation leakage-counters are added to the DREAM scintillation signal.

All of these data and simulations are consistent. In the next section, we perform a direct detailed simulation of the DREAM module *plus* the BGO array in front *plus* the large area scintillation counters surrounding DREAM .

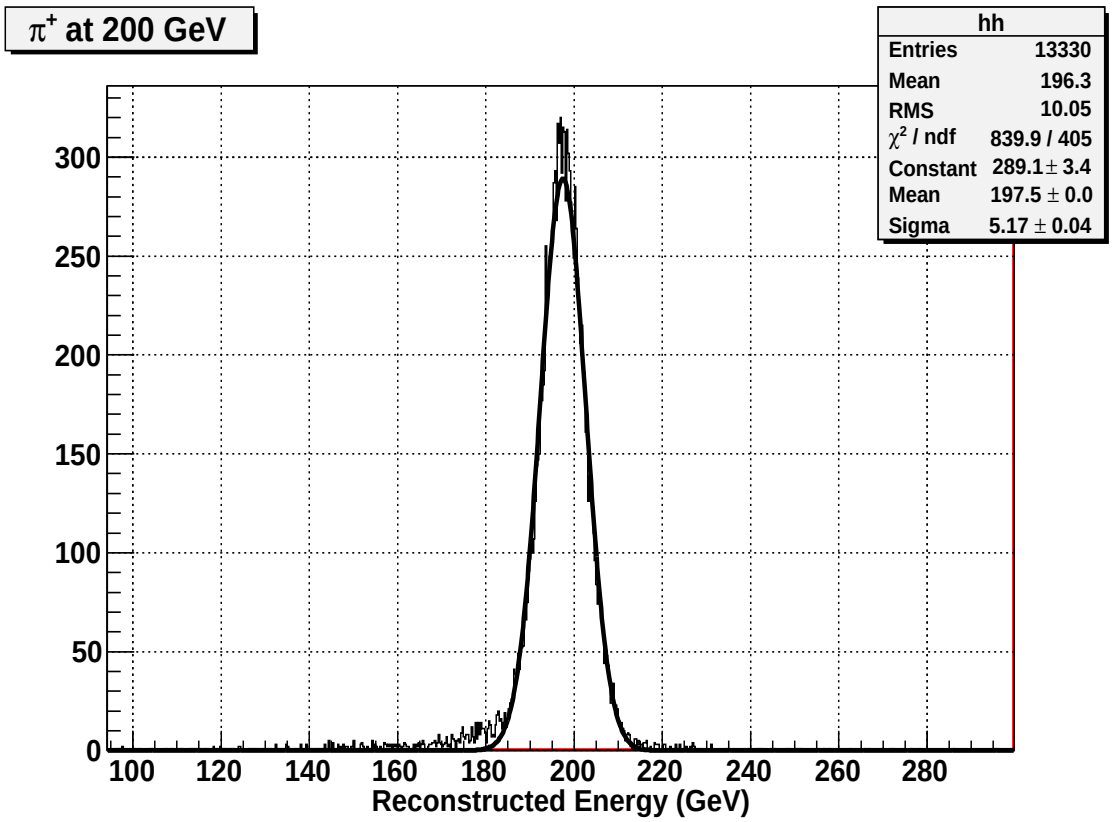

Figure 23: Dual-readout response of the 4th BGO+fiber calorimeter to 200 GeV π^- in ILCroot simulations.

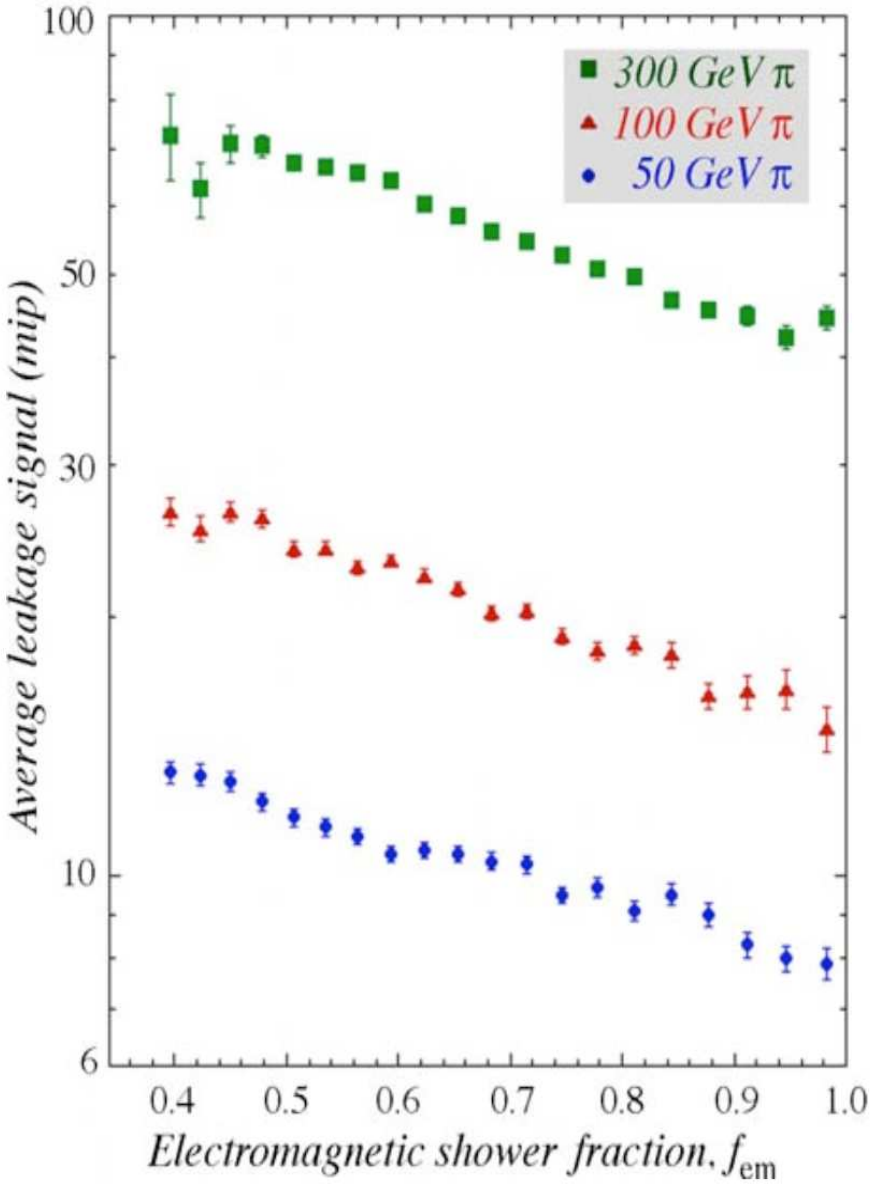

Figure 24: Leakage signal of mostly neutrons *vs.* the EM fraction in hadronic showers at 50, 100, and 300 GeV (DREAM data, submitted to NIM).

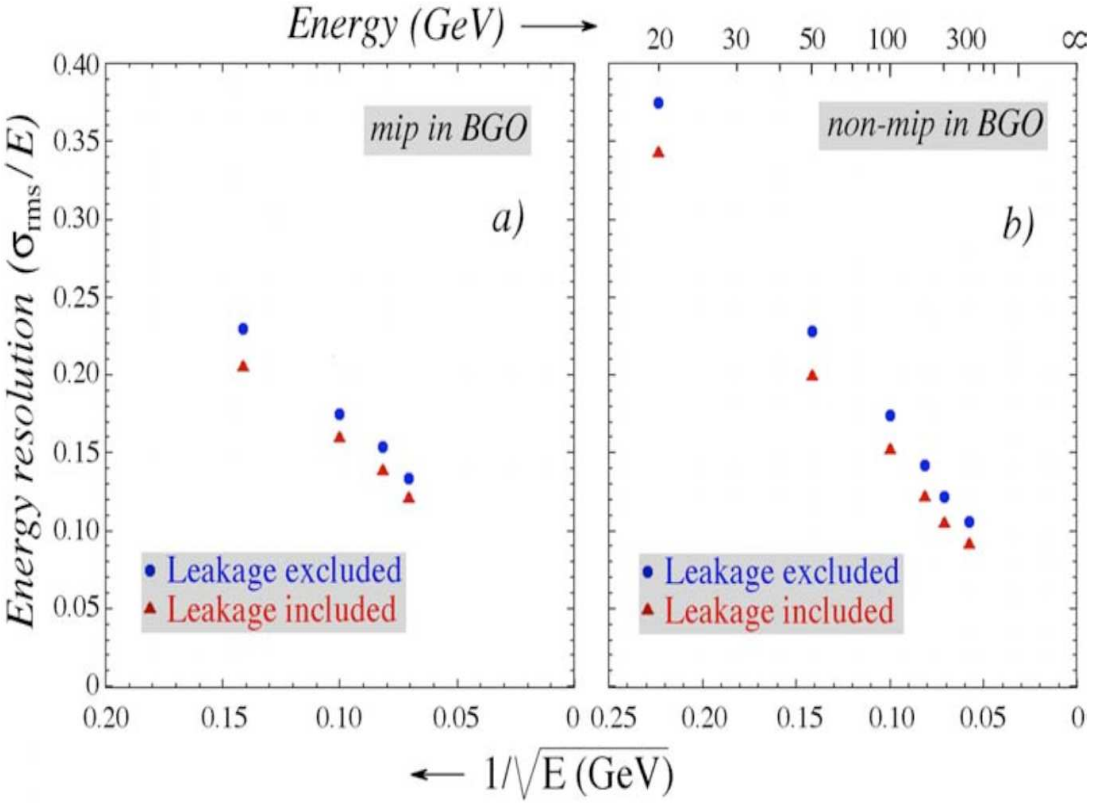

Figure 25: The energy resolution improvement attained by adding the leakage signal to the scintillations (S) signal of DREAM (submitted to NIM).

4.4.2 Direct simulation of the DREAM module: ILCroot 4th simulation

(Vito Di Benedetto, vito.dibenedetto@le.infn.it)

A direct and detailed simulation has been made of the DREAM module as tested in June 2004 and published "Hadron and Jet Detection with a Dual-Readout Calorimeter," N. Akchurin *et al.*, *Nucl. Instr. and Meths.* **A537** (2005) 537561.

Following figures are direct comparisons of DREAM data (top frames) and ILCroot simulation of the DREAM module (bottom frames). The quantities measured in DREAM and simulated with ILCroot are listed here:

Fig. 26 The mean scintillation signal as a function of $\pi^{\pm}$ beam energy.

Fig. 27 Scintillation signal *vs.* Cerenkov signal for 100 GeV pions.

Fig. 28 DREAM : Distributions of scintillation (S) and Cerenkov (C) signals for 100 GeV pions.

Fig. 29 ILCroot simulation: Distributions of scintillation (S) [top] and Cerenkov [bottom].

Fig. 30 Leakage-suppressed resolution function for DREAM data, (b) in upper frame, and ILCroot simulated resolution *using the same constants as used in data* to calculate the dual-readout energy.

Fig. 31 The dual-readout scintillation signal corrected for EM fraction (effectively a rotation in the S-C plane), for DREAM data (top frame) and ILCroot simulation (bottom frame).

Fig. 32 The non-dual-readout individual resolutions in the scintillation and Cerenkov signals from DREAM data (top) and from ILCroot simulations (bottom).

Fig. 33 Leakage-suppressed energy resolution for pions, in DREAM data (top) and in ILCroot simulations (bottom).

Fig. 34 The electron resolutions in the scintillation and Cerenkov signals from DREAM data (top) and from ILCroot simulations (bottom).

These extensive and detailed comparisons between data and simulations are extremely good. This is a direct simulation with the 4th ILCroot framework executing the FLUKA hadronic shower code. There is no such thing as "tuning a monte carlo" here. Just a direct instrument simulation.

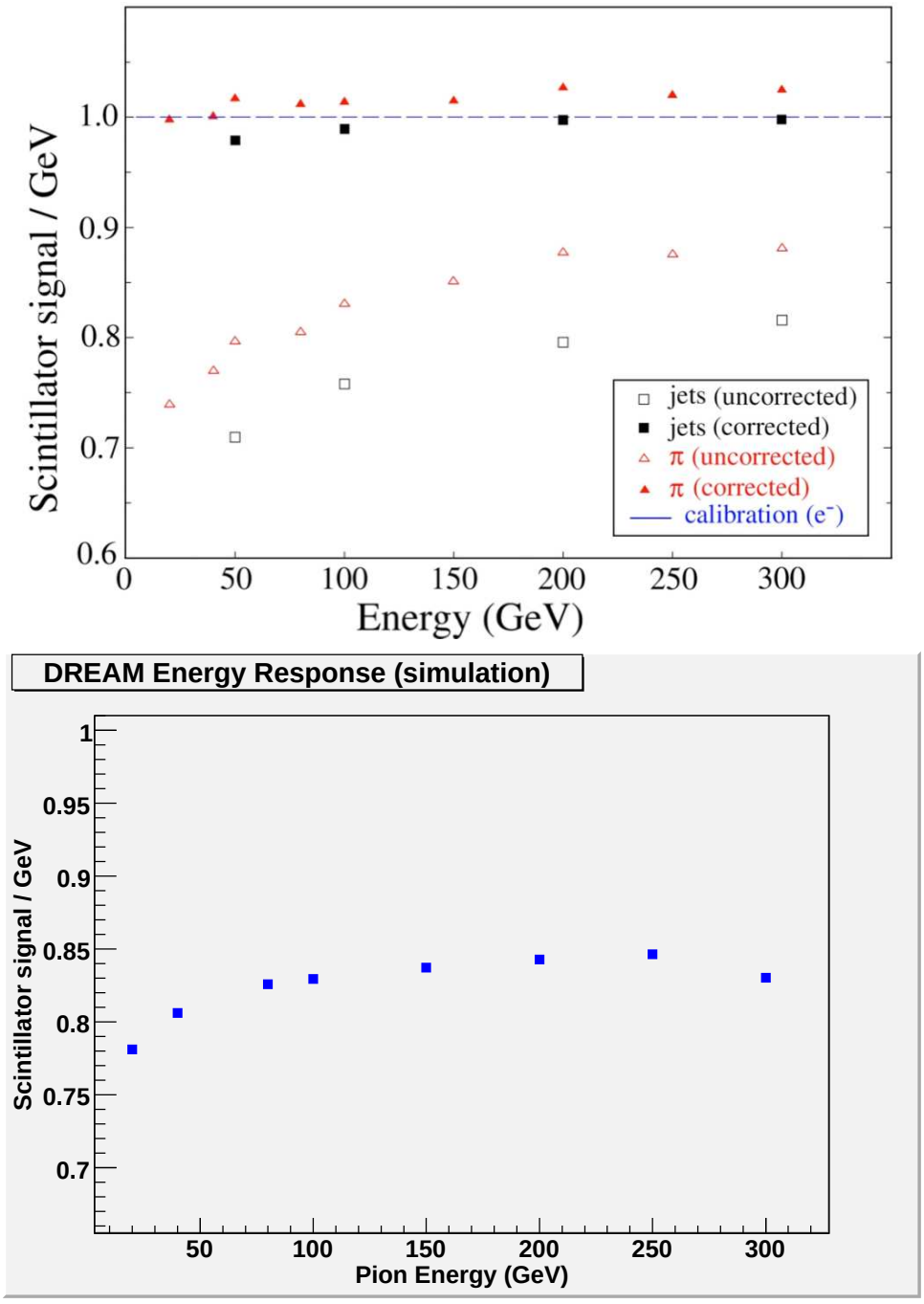

Figure 26: Average scintillation signal *vs.* pion beam energy: DREAM data (top), and 4th ILCroot simulation of DREAM (bottom). The ILCroot simulation should be compared to the red open triangles.

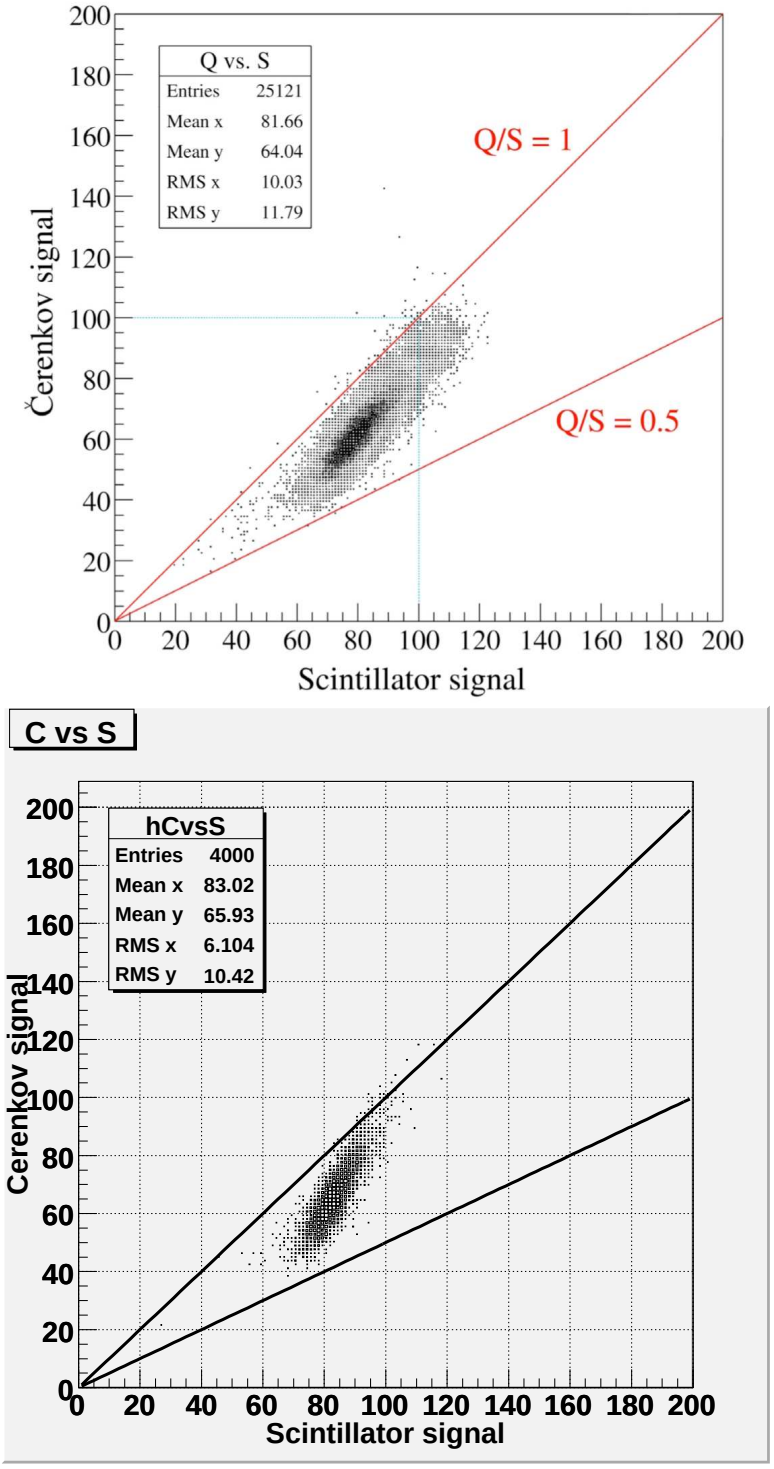

Figure 27: Scintillation signal *vs.* Cerenkov signal for 100 GeV pions: DREAM data (top), and 4th ILCroot simulation of DREAM (bottom).

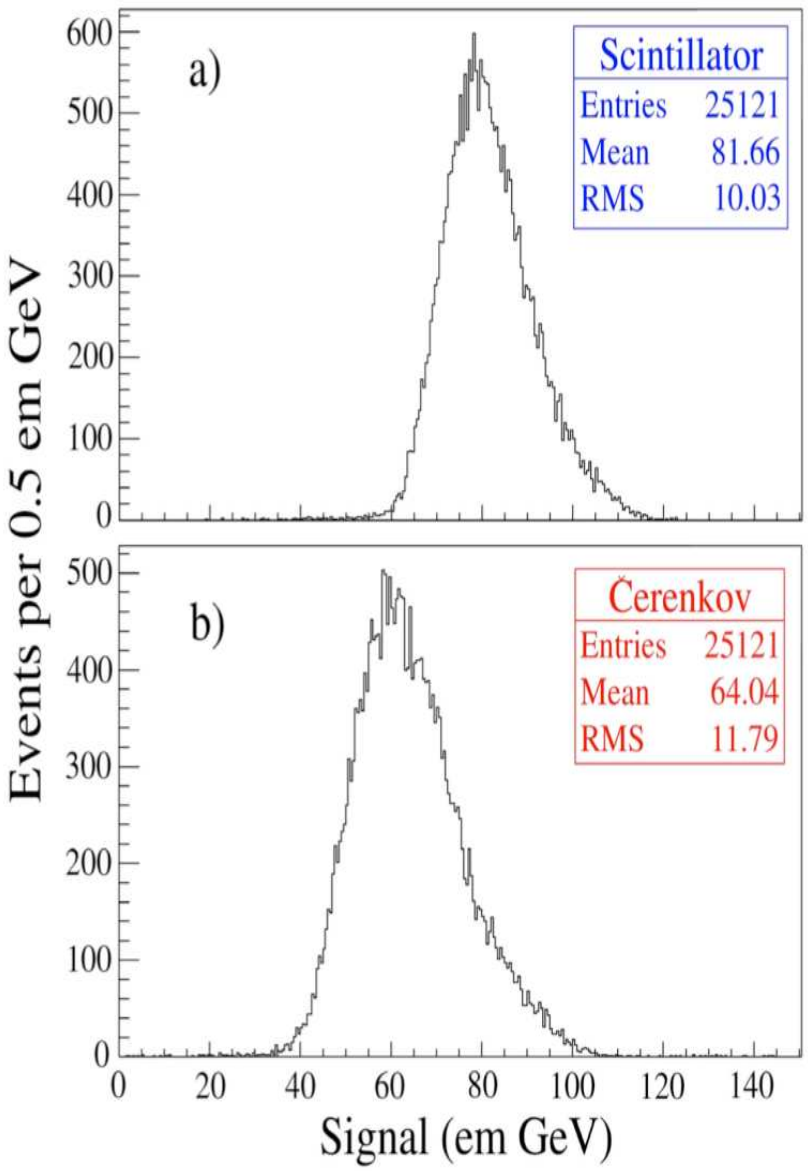

Figure 28: DREAM data: scintillation and Cerenkov signal distributions for 100 GeV pions.

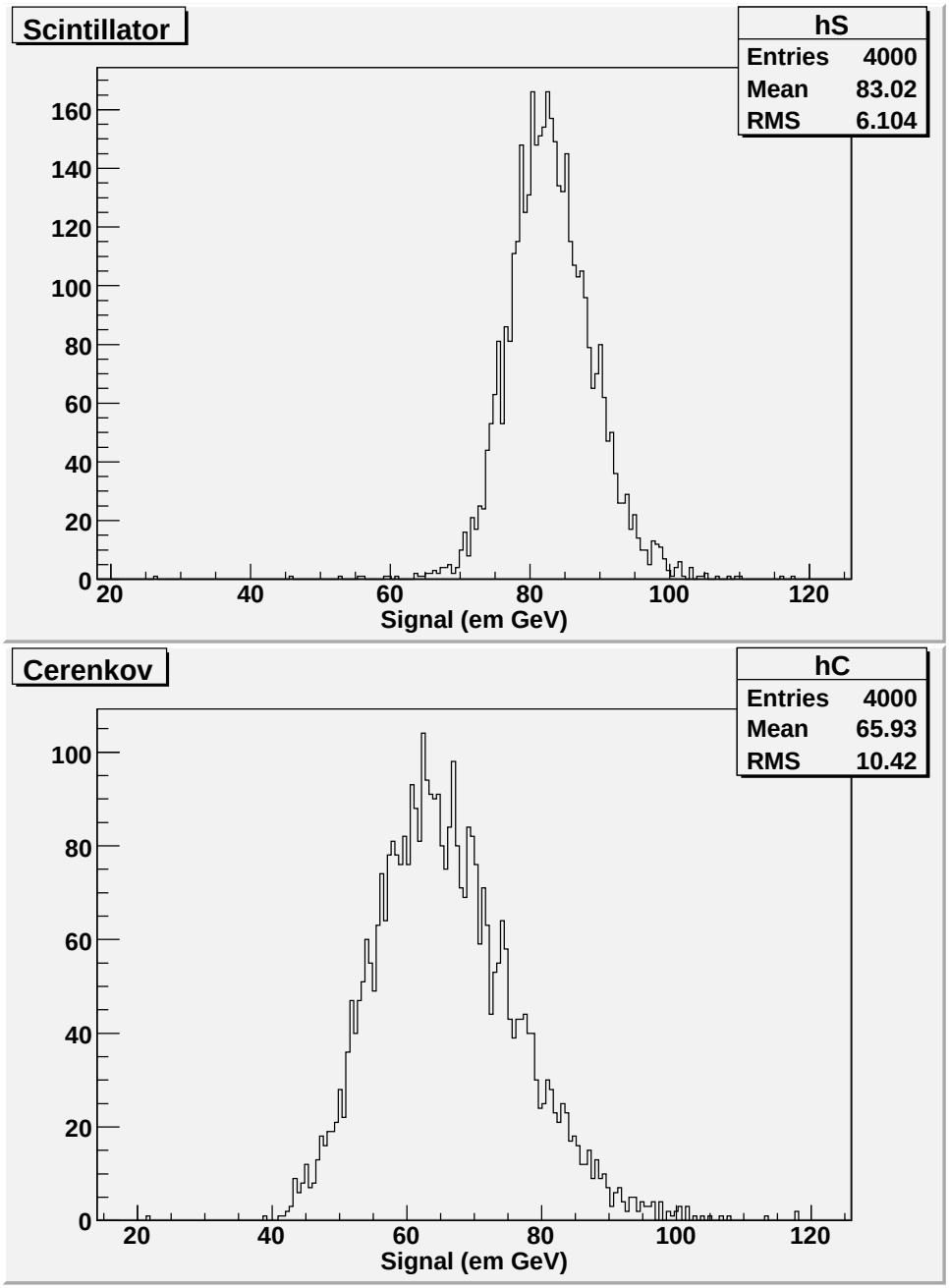

Figure 29: ILCroot simulation: scintillation signal and Cerenkov signal for 100 GeV pions.

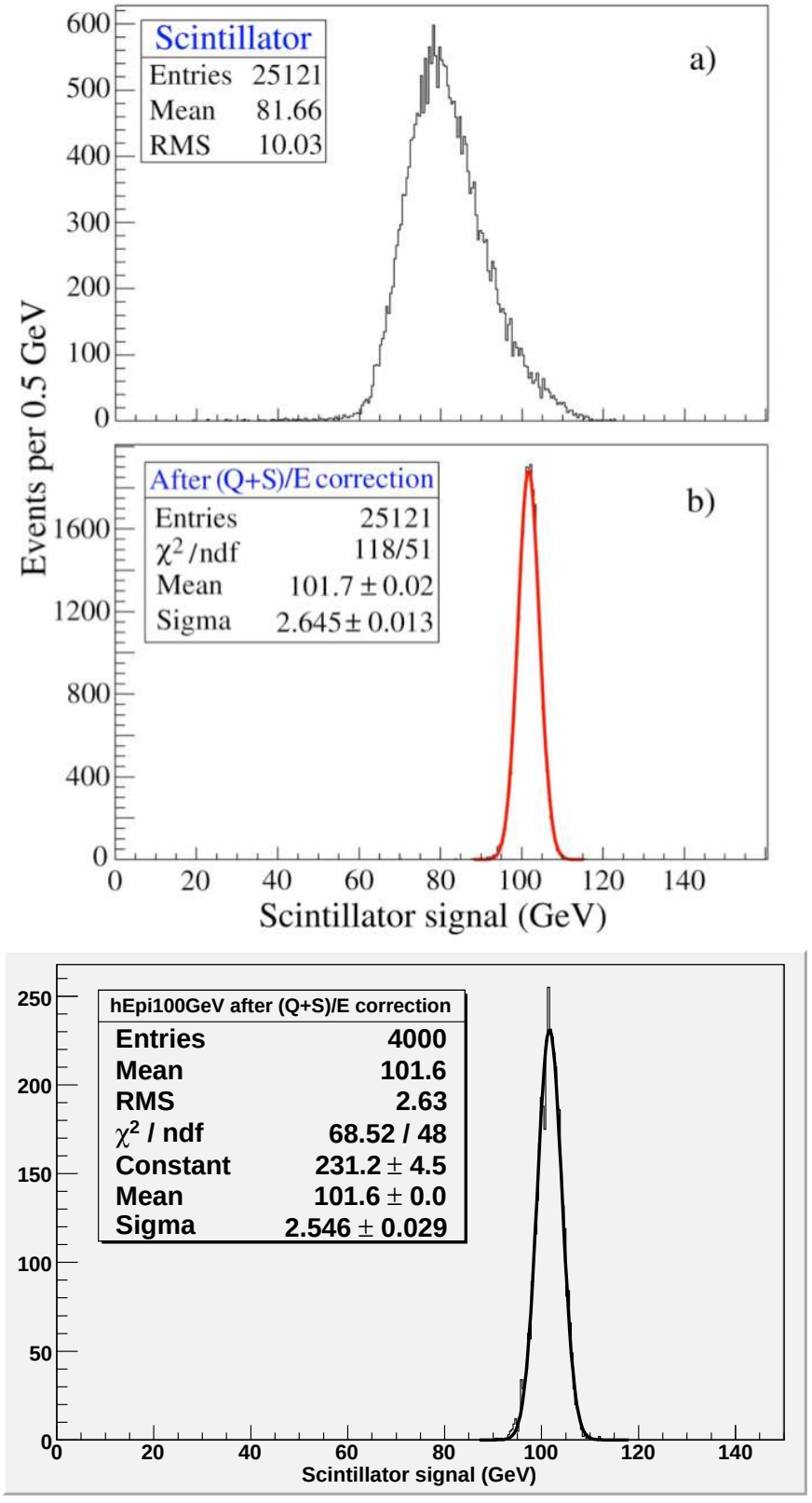

Figure 30: Leakage-suppressed resolution function for DREAM data, (b) in upper frame, and ILCroot simulated resolution *using the same constants as used in data* to calculate the dual-readout energy.

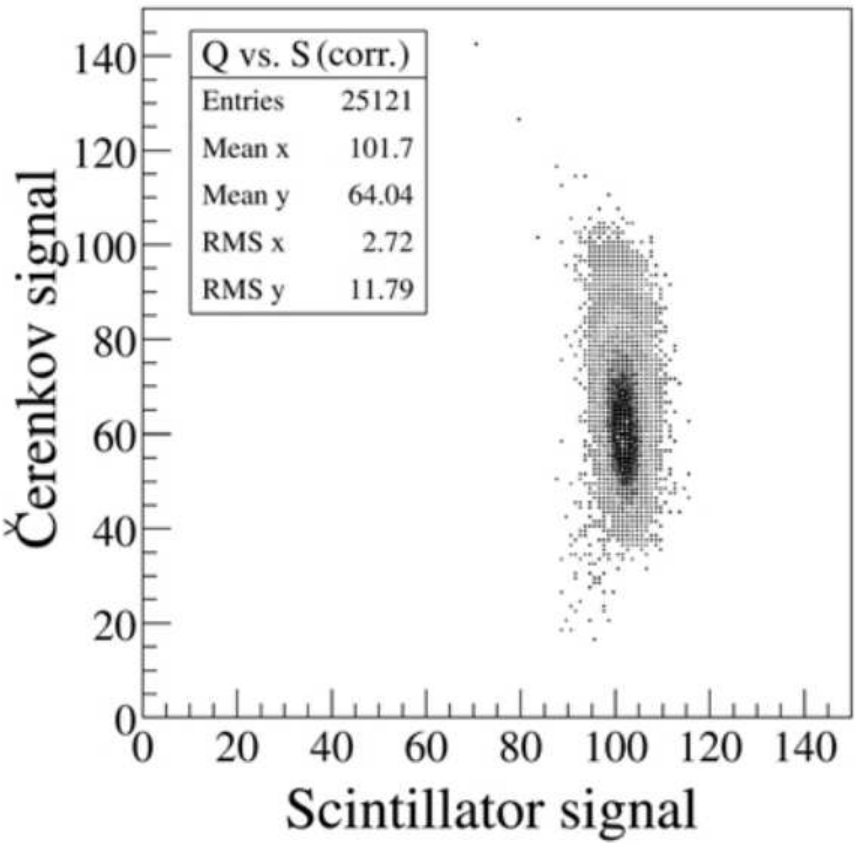

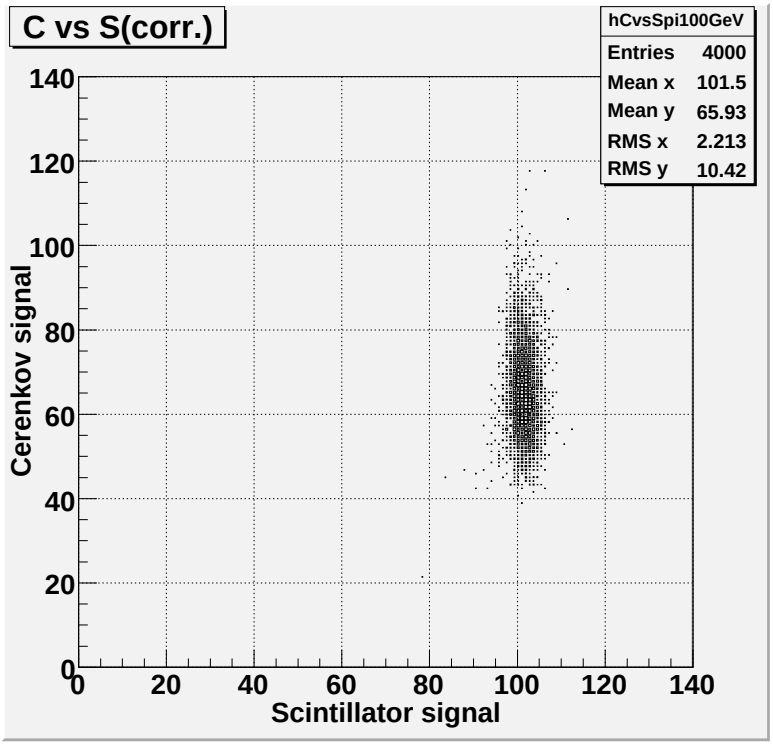

Figure 31: The dual-readout scintillation signal corrected for EM fraction (effectively a rotation in the S-C plane), for DREAM data (top frame) and ILCroot simulation (bottom frame).

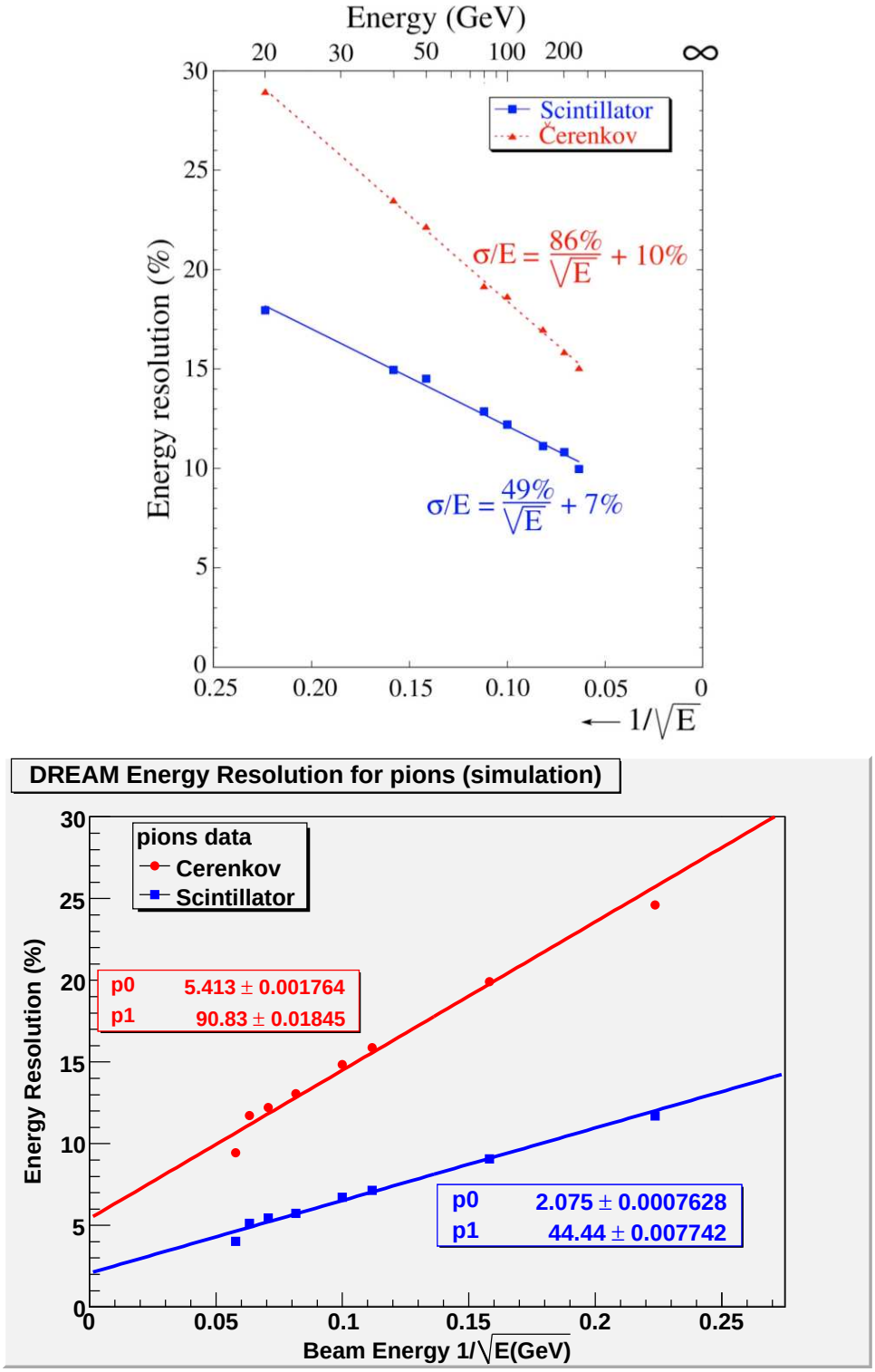

Figure 32: The non-dual-readout individual resolutions in the scintillation and Cerenkov signals from DREAM data (top) and from ILCroot simulations (bottom)

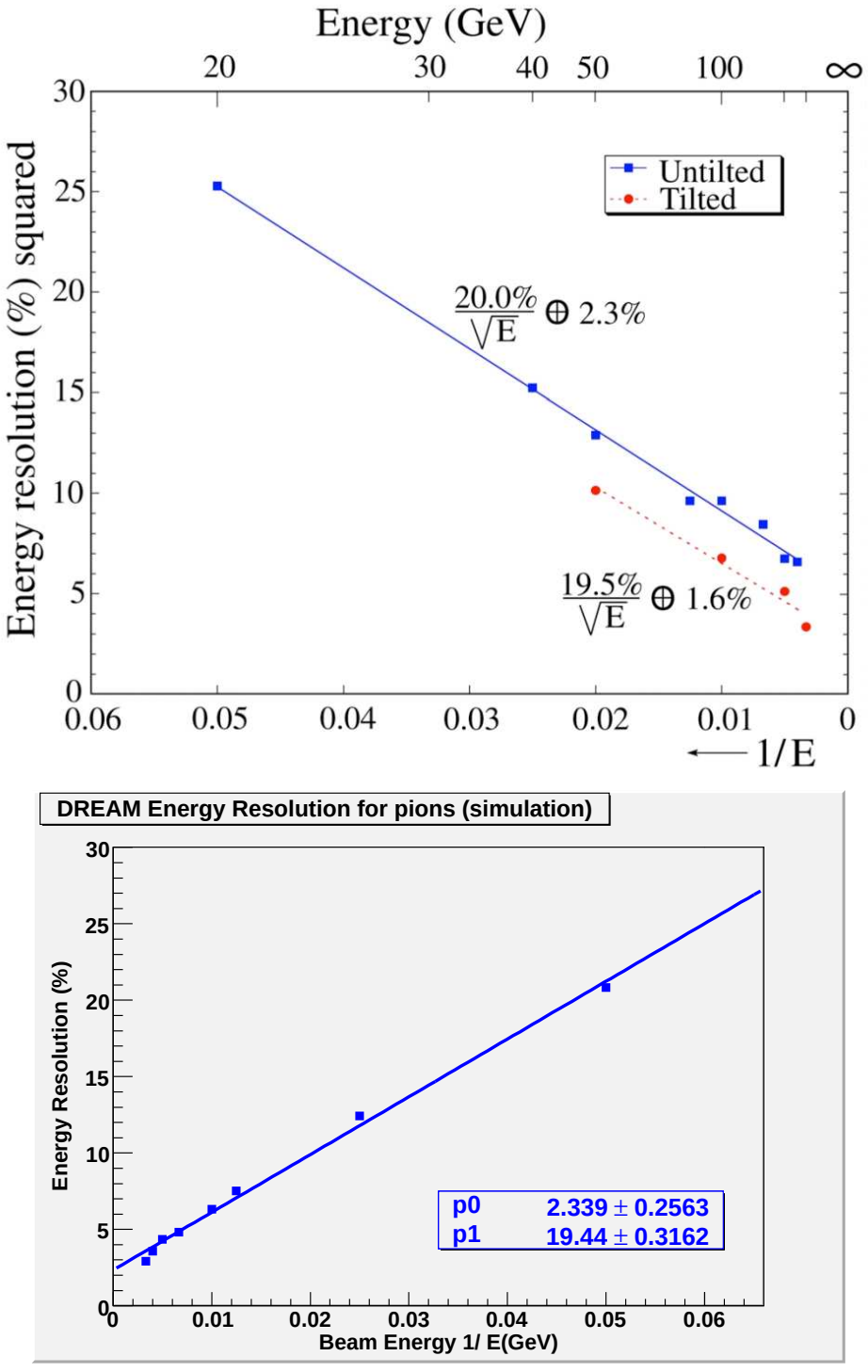

Figure 33: Leakage-suppressed energy resolution for pions, in DREAM data (top) and in ILCroot simulations (bottom).

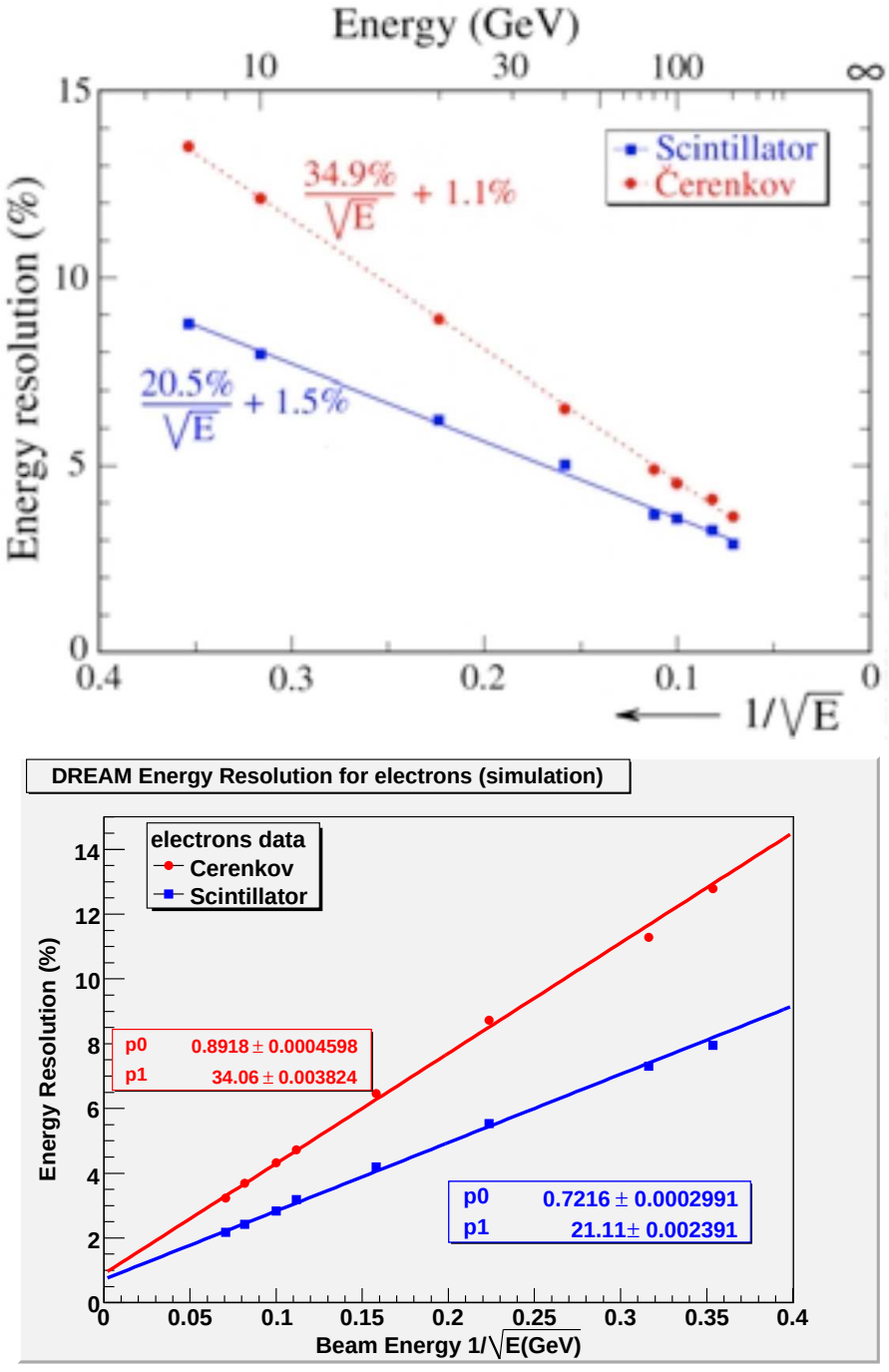

Figure 34: The electron resolutions in the scintillation and Cerenkov signals from DREAM data (top) and from ILCroot simulations (bottom)

5 MDI questions from Nobu Toge (18 May 2009)

5.1 Q1 - Numerics:

Please, check the summary table (MDIsummary.xls) and correct any factual errors, or provide the missing numbers, in particular, for the items that follow

Done.

5.2 Q2 - Footprint:

Please, indicate the envelope (or footprint) that the detector has to occupy during the maintenance period in the offline position.

The physical detector footprint is 12.15 m by 16.23 m, and adequate people-room for maintenance is 2 meters all around. The shielding footprint is 25.5 m by 30.0 m.

5.3 Q3 - Shield blocks:

Please, provide the rough size of additional shield blocks to use and their schematics (if they exist), when the detector is in the online position. The objects to consider include: pacmen, shield walls, others.

The individual shielding blocks in Fig. 37 are $200\times200\times1600$ cm^3 on the top, and $250\times250\times500$ cm^3 on the sides. Twelve long blocks are required, and the maximum mass to be lifted by a crane is 154 t. We could have a larger number of smaller pieces if this exceeds a reasonable crane capacity. Note that this 2 meter thickness is an overestimate of the required shielding, which is more like 1.5 meters (below).

The concluding plot for the shielding of 4th is shown in Fig. 35 from the three-LoI note "IR hall dose rate estimates with detector concepts," T.Sanami, A.Fasso, M.Santana, L.Keller, A.Seryi, S.Rokni, S.Ban, SLAC Radiation Physics Note, RP-09-08, March 30, 2009. A schematic of the shielding block arrangement is also (barely) visible in Fig. 35. This report concludes that

- The concrete with more than 1 m and 1.5 m thick for barrel and endcap, respectively, is required to reduce dose rate outside the 4th concept detector with realistic beam loss.
- The supplemental shield between DREAM calorimeter and pacman is remarkably effective to reduce dose rate around the 4th concept detector.

We include two further plots related to the shielding question and the PACMAN question in Figs. 36 and 37. These figures demonstrate *again* further advantages of an iron-free detector: easy movement of the hinging PACMAN doors, ease of access to the detector, no iron pole tips to obscure either a MONALISA laser viewing port or the movement and alignment of detector or BDS-FF elements.

Shielding Criteria: The limits of ambient dose rate are determined under three accelerator operation conditions, (S1) normal operation, (S2) mis-steering situation and (S3) system failure. For (S1) normal operation, radiation shield should be designed to satisfy ambient dose rate less than 0.5 μSv/h and 5 μSv/h for areas occupied by individuals who have license of general employee radiation training (GERT) and radiation worker (RW), respectively.

The shield has to assure that ambient dose rate is less than 4 mSv/h for areas occupied by individuals under (S2) mis-steering situation.

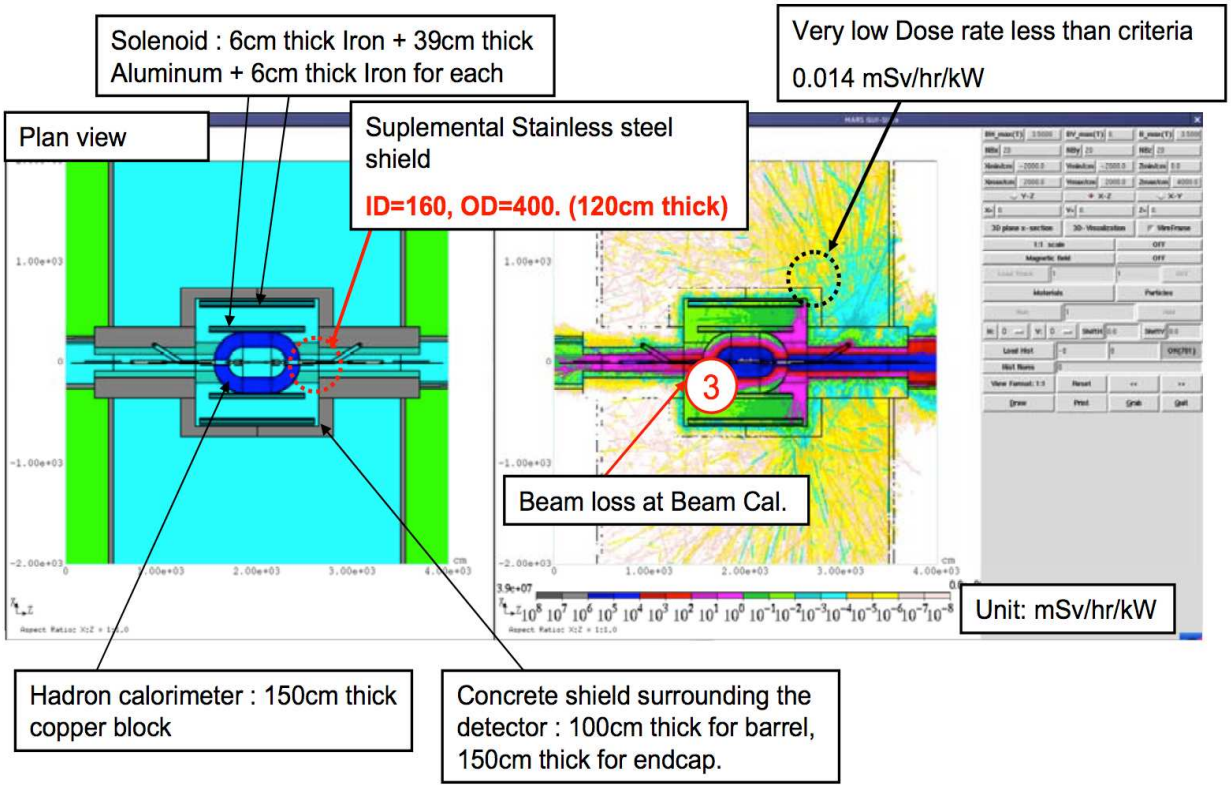

Fig 3-12-2 Plan view and dose rate distribution in experimental hall for 4th concept detector with supplemental stainless steel shield. The shield thickness is 120 cm.

Figure 35: Shielding for 4th yields dose levels below the most stringent criterion at the worst position. This calculation is done by T. Sanami, *et al.*.

For both (S1) normal operation and (S2) mis-steering situation, annual integrated dose should be less than 10 mSv/year.

Concerning (S3) system failure case, ambient dose rate should be less than 250 mSv/h outside shielding wall for maximum credible beam loss. Integrated dose rate per event is also limited under 30 mSv/event.

5.4 Q4 - Platform and height:

Please, indicate the assumed height of the platform beneath the detector, its size, its weight, and the assumed beamline height relative to the detector hall floor.

The weight of the platform is about 150 t when made from Al with a filling factor of 8%, and its dimensions are 25.5m by 30.0m and 1.5 m thick. The beam line height is 9.5 m above the cave floor. We are flexible on this matter, but it will not differ much from ILD or SiD, and it will be established with the complementary detector.

5.5 Q5 - Gross weight:

Please, indicate the gross total sum of the weight of your detector system, including the barrel, endcaps, platforms (if any), and shield blocks.

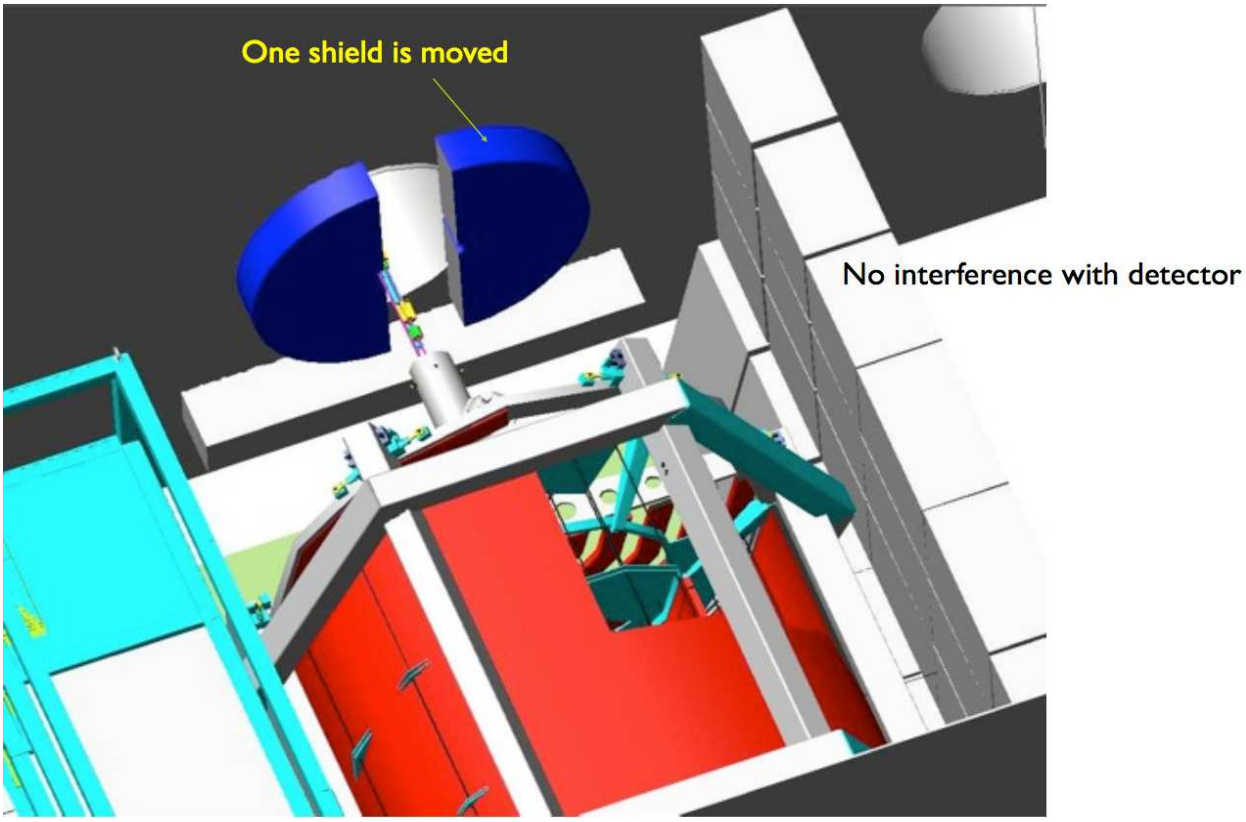

Figure 36: PACMAN positioning and movement in 4th. Note one further advantage of an iron-free detector: the PACMAN movements are free and unhindered by iron pole tips or any other part of the detector.

component	volume (m^3)	density (t/m^3)	mass (t)
barrel calor. (80% Cu, 20% fiber)	38	8.9	300.
End calor. (80% Cu, 20% fiber)	38	8.9	300
solenoids (1/2 CMS)			100
supports			63
shielding blocks	600	2.4	1440
platform	2	6.0	12
Total mass of 4th (t)			2200

5.6 Q6 - QD0:

Please, indicate the Z locations of your QD0 (Zmin and Zmax) and their radius R to occupy.

Figs. 41 and 40 show these dimensions and we include them in the following Table.

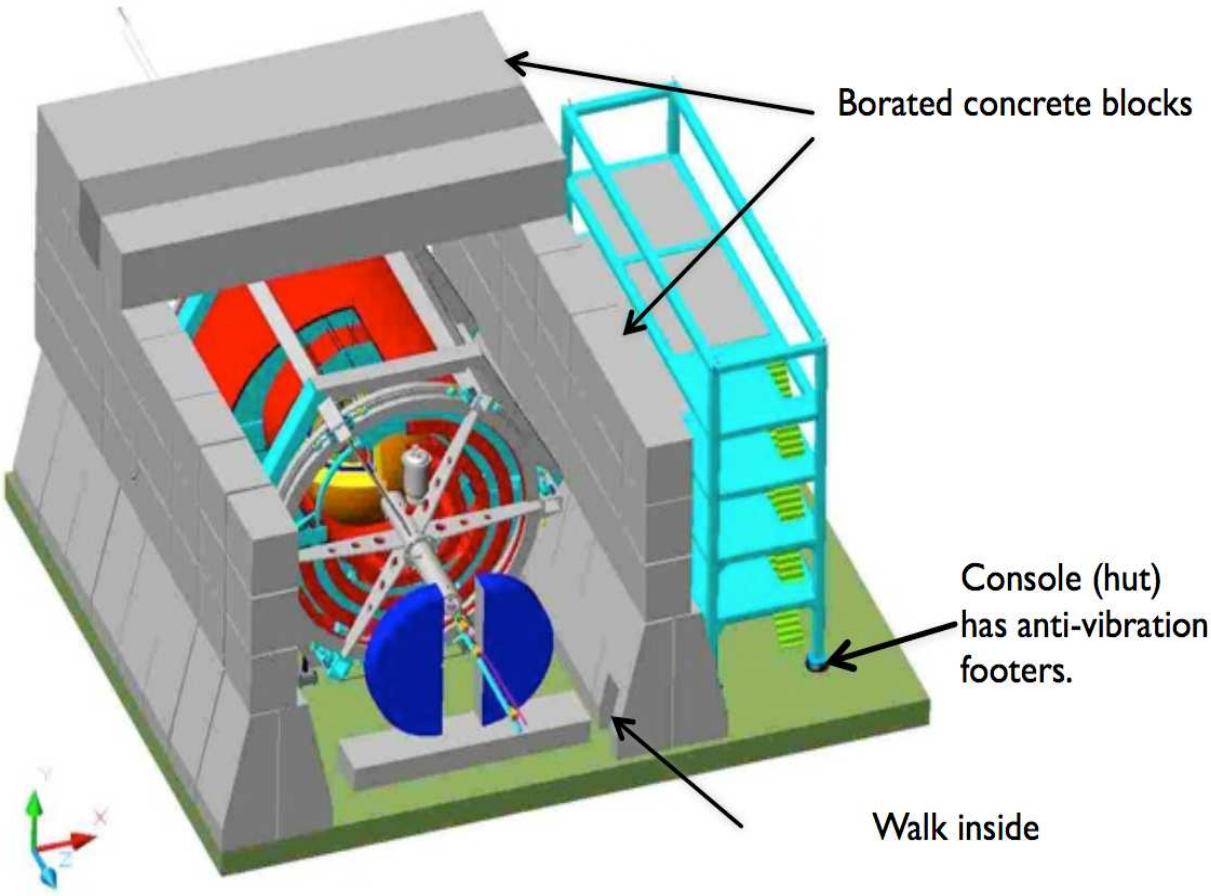

Figure 37: View of the concrete and borated carbon shield of 4th. Note the easy access to the detector without the iron mass.

elements	$z_{\min}$ (cm)	$z_{\max}$ (cm)	radius (cm)
D0,QC0,SD0,QDEX1	450.	800.	20.
QF1,SF1,QC1,QFEX2	950.0	1188.0	20.

5.7 Q7- Cryogenics:

Please, indicate if your QD0 and the solenoids are to operate at 2K or 4K.

We plan to operate QD0 and the dual solenoids 4.2 K.

5.8 Q8 - Push-pull motion:

A view of 4th inside its shielding and on a platform with rollers is shown in Fig. 38. Dimensions and distance for the shielding blocks, the beam height above the cave floor, the platform thickness,

and the footprint are shown in the figure. These shielding blocks are 2 meters thick, although only 1.5 meters is required. Furthermore, we will seek to deepen the calorimeter to lower the amount of shielding concrete needed.

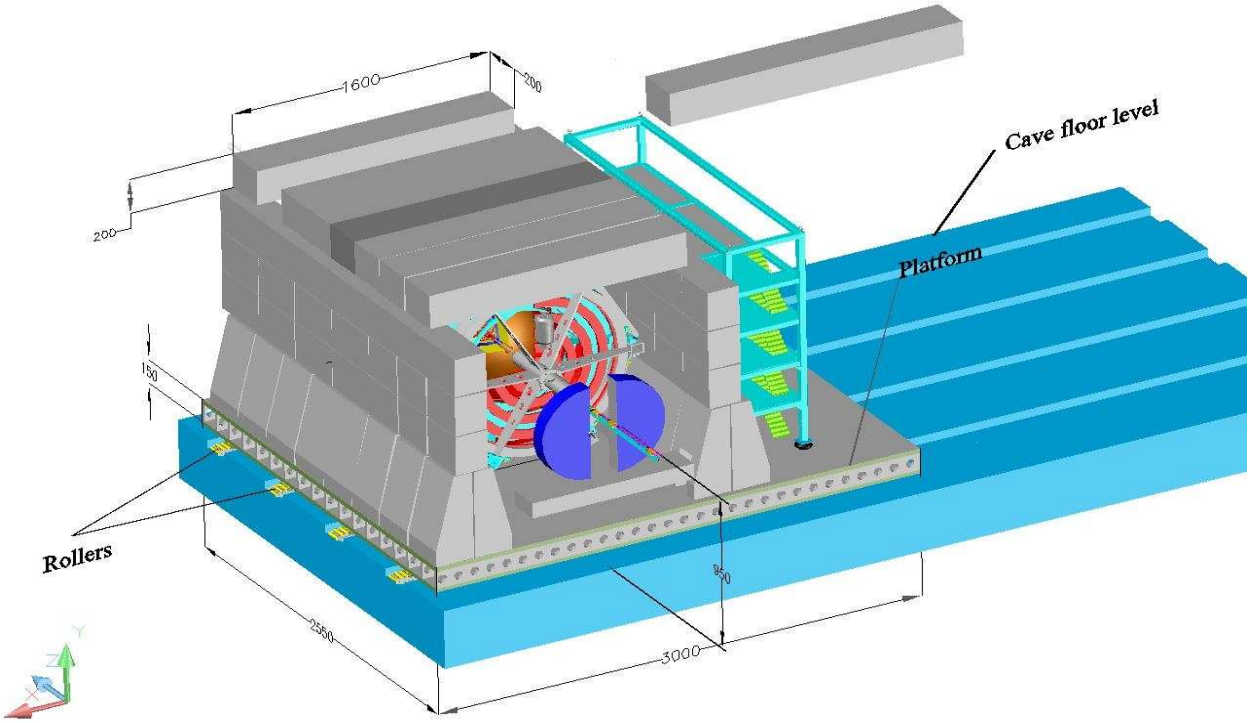

Figure 38: The 4th detector on its platform inside its shielding and on rollers for push-pull.

Q8(a) *Please, indicate the preferred method of push-pull motion mechanics that is currently under consideration.*

Our preferred push-pull method will use the same system as the other (complementary) detector for unification and cost reduction. 4th is rather flexible in this matter due to its light weight. Currently, we are considering a strategy in which 4th moves on a platform for faster in/out movements, and the platform rolls on appropriate rollers. As far as the common platform option, this needs to be evaluated carefully, since locating two detectors on a common platform makes protection against vibration more difficult. If the detectors are on a common platform, then mechanical activity in the other detector region (which is in the "off" position) inevitably transfers to the first one. Activities in off detector might include disassembling a part of its yoke, so perturbations could be significant and unpredictable. In fact, vibrations of any kind on the other detector could raise problems with luminosity stability. So the basic approach we take is that the tracks, platform thickness and rollers could be uniform for both detectors, but the platforms are separate.

In this case of two platforms, one for each detector, the actual push could take place when the two platforms are linked together, making one semi-rigid platform that would be pushed from the

left, and then pushed from the right.

Q8(b) *Please, identify the hardware components (beamline elements, shield blocks, and utilities) that need to be disconnected/disassembled and reconnected/reassembled during your detector push/pull. Please, estimate how long this relocation / reassembly work will take.*

We will have to disengage the QD0-QF1 flange (but, only if the other detector chooses to keep QF1 attached to the IR). Otherwise, the whole detector including cryo connections remains connected. We have not made a credible (and independent) estimate of push-pull time, but will rely on the estimates of the other two concepts. In the end, 4th is simpler with fewer subsystems, fewer channels (by a factor of 10^3), and less massive by a factor of 5. All of these give us confidence that if a solution exists for ILD or SiD, it will exist for 4th.

For the shielding blocks, basically all blocks remain on the platform. Only those blocks on the edges of the platform that might interfere with platform motion would need to be removed. The likely case is that no block needs to be moved.

Q8(c) *Assuming that the accelerator (including QF1) is in a good alignment condition, how long would it take to complete your detector push, and complete the alignment of the detector components. Explain how you will do this realignment; i.e. what kind of measurement and mover systems.*

The final realignment will use low-intensity beam mode for active alignment using the readings from BPMs and the deflection of the beam trajectory if the beam is running through off center in the quadrupoles and sextupoles. We will calibrate pickup electrodes for zeroing their signals if the beam is running through the quads axis. This was successfully tested at the FFTB.

The FFTB ((Final Focus Test Beam, *Phys. Rev. Lett.* **74**:2479-2482,1995) developed all the techniques we need, except we will incorporate the newly developed MONALISA positioning system. After QF1 is positioned, we will

1. align QD0 (both sides) and its sister elements;
2. align the sextapoles and kickers. Use BPMs at start of alignment, transition to MONALISA at end of alignment.
3. BGO calorimeter is on, providing a perfectly adequate monitor of collisions which result in energetic tracks. All other systems are off for safety, and the fiber calorimeter is off because it is less necessary.
4. the pixel vertex remains mostly aligned with QD0 (another benefit of a central FF support that is attached to the detector), but will have its own MONALISA for highly accurate alignment;
5. it is expected that the alignments of the tracking chamber and the calorimeters (and muon spectrometer) will have changed during the push-pull. These are measured with a MONALISA, but not aligned, since the reconstruction codes can easily handle mis-alignments of 1-100 μm;
6. pixel vertex, tracker, BGO and fiber calorimeters are finally aligned with tracks from the IP.

Many of these movements will be concurrent since, *grosso modo*, the detector which must be internally aligned need not be absolutely positioned with respect to the collision IP.

Q8(d) *How long would it take to complete your detector pull and to make the interaction region and the BDS ready for the other detector?*

If we must disconnect the QD0-QF1 flange, this will be 2 hours, unloading a few blocks will be 2 hours, then the only remaining time is the movement of the common platform (about 1 hour) which is concurrent in time with the other detector's push. We now think that the total pull time for 4th is below 6 hours.

Q8(e) *During the upcoming Technical Design Phase, what type of resources do you plan to allocate for the conceptual and engineering work on MDI-related issues, and how you intend to operate them? Also, do you have any requests for assistance to the RD management or to the MDI group, in terms of resource sharing or in terms of interactions on technical matters?*

Clearly, 4th is not a big lab. Given even moderate resources, we can employ physicists and engineers at Fermilab, or even do common work with SiD, on MDI and beam issues.

5.9 Q9 - (for 4th) QD0-QF1 separation:

4th is known to prefer holding QD0 and QF1 together on the detector, but separating them is not completely excluded, as we understood in the discussion at TILC09. In that case, please, give a sketch description as to what the QD0 / QF1 support systems would be like when you separately hold the QD/QF magnets for the 4th detector system.

We will show several figures for this discussion, but we note that this 4th proposal is beneficial to all concepts and not restricted to 4th in any way (due to its lower mass, for example). Our main conclusion is stated here and backed up by the FF calculation "Final Focus Lens Stability," A. Mikhailichenko available in Appendix A of the 4th LoI (file "A.MDI-Mikhailichenko-stability-final-doublet-lenses.doc" at www.4thconcept.org)

> We believe that a detector without QD0 and QF1 mounted on a common detector frame will not work, that is, the vertical jitter is about 13 nm, corresponding to a miss of the bunches. Mounted on the same frame, the vertical jitter between both beams is highly correlated and luminosity will be maintained.

Fig. 39 shows the two proposals (4th and non-4th): on the right is the current non-4th MDI proposal for QD0 and QF1 on separate mounts. On the left is the 4th proposal for a common mount of both QD0 and QF1, in this drawing the flange shown is used to connect the quads after a push-pull.

A detail of the support frame for QD0 and QF1 is shown in Fig. 40 with all important FF components inside the common support tube that is connected to the other side of the detector by a common detector frame. The flange is located at a convenient position for disconnect between QD0 and QF1. The incoming and outgoing beams are shown, along with QD0, QC0, SD0, QDEX1, the feedback kicker, QF1, SF1, QC1, and QFEX12.

The axial and radial dimensions of 4th and the axial locations of the flanges and the axial extent of the FF are shown in Fig. 41 and summarized in the Table:

L^*	300.0 cm
Radial extent	607.5 cm
Axial location of flange	811.5 cm
Axial extent of FF	1188.0 cm

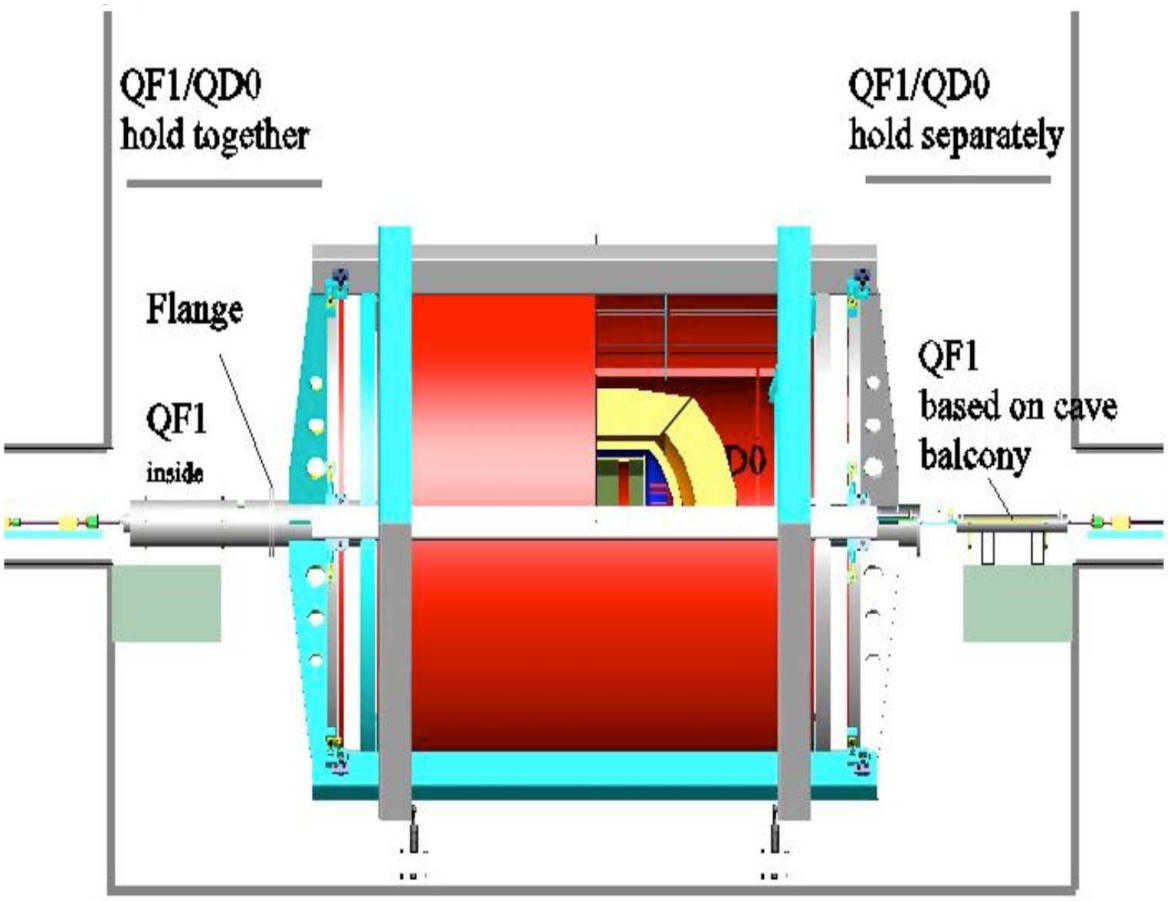

Figure 39: Drawing of 4th with QD0 and QF1 mounted on the same frame on the left side showing the flange that would connect them; and, the present MDI proposal of separate supports for QD0 and QF1.

The active supports developed in the FFTB program at SLAC are illustrated in Fig. 42, in which the two magnetic element trains [QF1, SF1, QC1, QFEX2] and [QD0,QC0,SD0,QDEX1] are aligned and positioned by the active movers. The positions of these components are continuously monitored by a MONALISA system with relative ease since there are no iron pole tips to obscure a straight-line laser view in this important region of the detector.

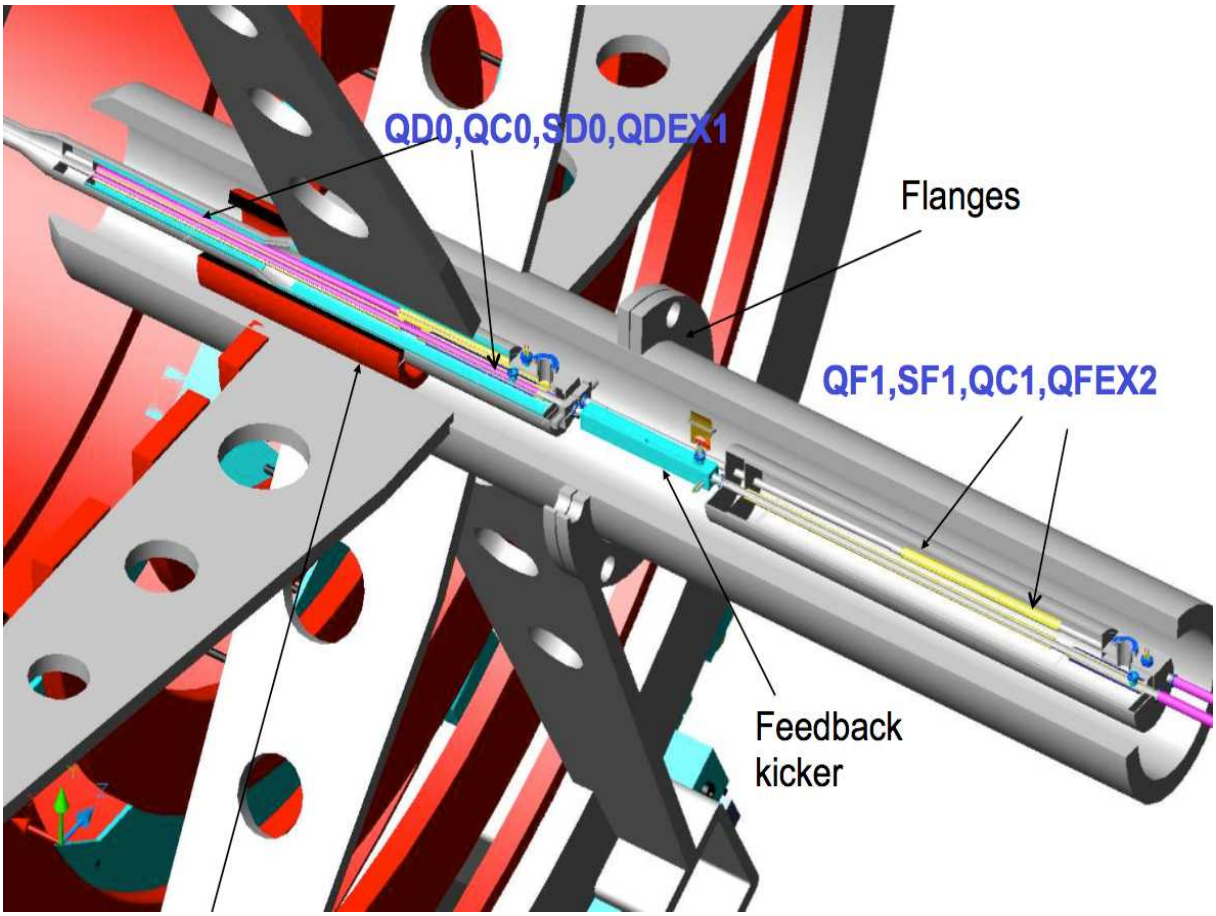

Figure 40: Detail of the support of QD0 and QF1 on a common frame that is supported by the detector. The flange between QD0 and QF1 is shown, along with the radial supports that make this one support frame be integral with the FF on the other side of the detector.

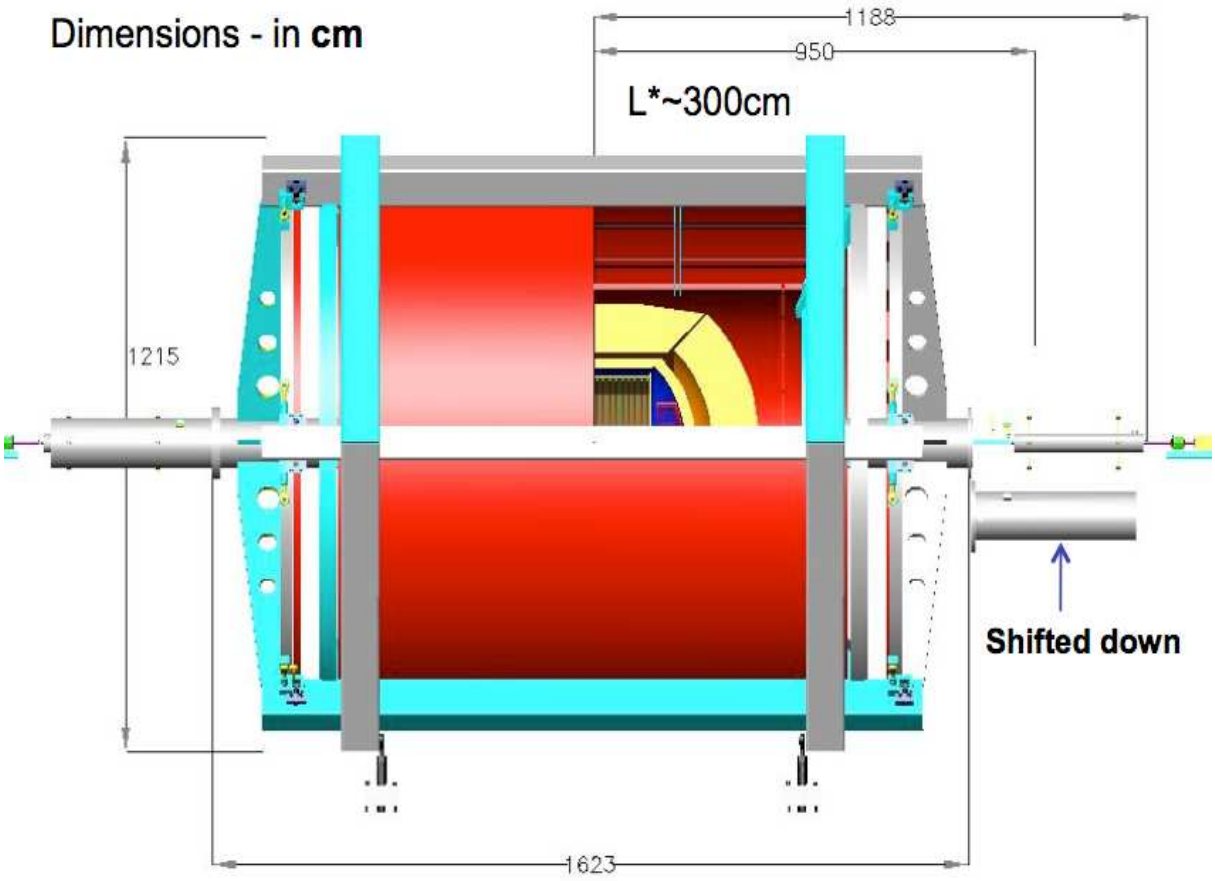

Figure 41: The large-radius flange that would rigidly connect QD0 (part of 4th frame) and QF1 (part of IR/linac) together at the end of the push-pull operation.

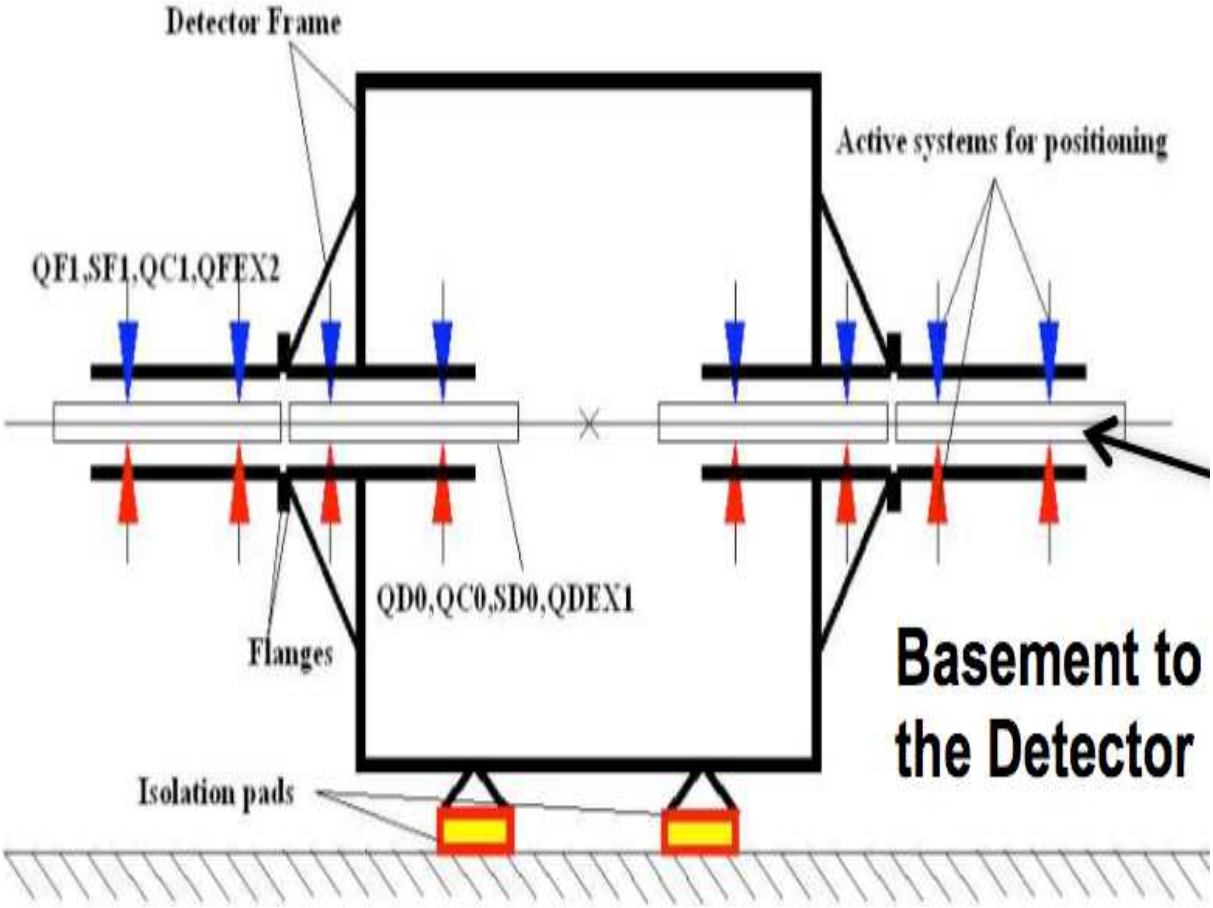

Figure 42: Drawing showing the active movers and support of the single piece [QF1+QD0+detector+QD0+QF1]. The alignment and positioning were well established in the FFTB ("Final Focus Test Beam") and we would use the same or similar devices.